Available online at www.sciencedirect.com

ScienceDirect

Comput. Methods Appl. Mech. Engrg. 275 (2014) 234–263

Computer methods in applied mechanics and engineering

www.elsevier.com/locate/cma

Discrete micromechanics of elastoplastic crystals in the finite deformation range

Ronaldo I. Borja *, Helia Rahmani

Department of Civil and Environmental Engineering, Stanford University, Stanford, CA 94305, USA

Received 22 October 2013; received in revised form 23 February 2014; accepted 4 March 2014
Available online 19 March 2014

Abstract

We present a rate-independent crystal plasticity theory in the finite deformation range. The formulation revolves around theory of distribution and strong discontinuity concepts applied to the slip systems. Uniform and conforming deformation fields are introduced, from which deformation gradients for the crystal lattice and the crystal itself are derived. For a crystal deforming in single slip, we show that the crystal rotates the active slip system the same way as the lattice does, leading to an elegant and exact stress-point integration algorithm for the overall crystal stresses. For a crystal deforming in multiple slips the crystal no longer rotates the slip systems exactly as the lattice does. For this case, we present a stress-point integration algorithm accounting for the exact push-forward operation induced by the lattice on the active systems. We also consider a simplified stress-point integration algorithm for multislip systems that remains highly accurate for a wide range of stress paths considered. The framework for system activation and the selection of linearly independent slip systems follows a well-established 'ultimate algorithm' for rate-independent crystal plasticity developed for infinitesimal deformation.

Keywords: Crystal plasticity; Finite deformation; Micromechanics; Stress-point integration; Strong discontinuity

1. Introduction

Quasi-static and isothermal plastic deformations in single crystals arise from slips on specific crystallographic planes. Certain crystalline solids, such as metals and igneous rocks, have well-defined microstructures that allow modeling of their mechanical responses based on grain-scale mechanisms. One of the first representations of metals as a polycrystalline aggregate was proposed by Bishop and Hill [7,8]. They employed the notion of plastic work to describe yielding of the polycrystal, but neglected the elastic strains and did not address the sequence of slip system activation. Since then, several other developments have been published

* Corresponding author. Tel.: +1 6507233664.
E-mail address: borja@stanford.edu (R.I. Borja).

http://dx.doi.org/10.1016/j.cma.2014.03.002
0045-7825/

in the literature, most of which have focused on identifying the set of linearly independent active systems from a pool of linearly dependent ones [16,17,20,26,30,33,34,37]. Identifying linearly independent systems is a fundamental problem because redundant systems lead to indeterminate slips.

The most common algorithm for filtering out redundant constraints emulates the return mapping scheme of multisurface plasticity [20,23,58]. In this algorithm, redundant slips systems are identified from the zero elements of the factorized coefficient matrix, which are then dropped from the set of potentially active constraints during the course of the iteration [1,20,54,58]. The return mapping algorithm for multisurface plasticity is known to work well for problems where the constraints are all linearly independent; however, for problems involving linearly dependent systems this algorithm could break down even at the stress-point level [16]. Borja and Wren [16] proposed an 'ultimate algorithm' for tracking the sequence of activation of linearly independent slip systems. Their work is unconditionally convergent and exact for loads varying as a ramp function, and has recently been implemented into a 3D nonlinear finite element code addressing infinitesimal deformation [9].

Rate-dependent regularization has been employed to avoid dealing with linearly dependent slip systems [19,31,44,50,59]. In rate-dependent formulation, all systems can be active, and slips are determined according to the viscosity of the material. A rate-dependent formulation could be justified by the plastic flow due to dislocation motion being inherently rate-dependent [48,51]. However, when the rate sensitivity becomes small the resolved shear stress becomes a bounded function, making the set of constitutive equations exceedingly stiff and very difficult to solve [22,39]. In such cases, it may be more expedient to formulate the problem as a rate-independent one and develop an algorithm for this specific class of problems. Among the rate-independent plasticity formulations reported in the literature, we mention the ultimate algorithm by Borja and Wren [16], the generalized inverse approaches by Anand and Kothari [1] and Schröder and Miehe [54], the smoothed yield surfaces of [25], and the diagonal shift method by Miehe and Schröder [45]. For a more in-depth discussion of the issues surrounding this topic, the reader is referred to [18].

Consideration of finite deformation effects is required in the simulation of metal forming and the analysis of localization of deformation in geologic crystalline materials, among many applications of crystal plasticity [21,32,46]. Within the framework of nonlinear continuum mechanics, various formulations for crystalline materials experiencing large elasto-plastic deformation have been proposed [4,5,28,53]. The most commonly accepted framework revolves around the notion of multiplicative decomposition of deformation gradient [36]. Under conditions of multiple slips, the plastic component of velocity gradient obeys the flow rule presented by Rice [53]. Due to redundant slip systems, selection of linearly independent systems from a pool of linearly dependent ones continues to be a major challenge. Furthermore, the presence of geometric nonlinearity requires a more elaborate mathematical description of the nonlinear kinematics of crystalline slips. Factors entering into the kinematical description include the rotation and stretching of the crystal lattice and the large magnitude of crystal slips.

Crystals exhibit significantly higher hardening rates when deforming in multiple slips than when deforming in single slip [6]. This implies a strong propensity of the crystal to deform in single slip and avoid multiple slips. A strong latent hardening captures this pattern of deformation and is the main feature of a subgrain dislocation model [50]. Because of the dominant role of single slip in crystal deformation, an accurate numerical algorithm that captures the kinematics of deformation in single slip is desirable. On the other hand, single slips at all material points are known to result in a non-convex incremental problem—unless multiple slips are also allowed, or unless the crystal is permitted to develop some deformation microstructures such as 'patchy slips' [4]. These overarching considerations motivate the development of a finite deformation stress-point integration algorithm for a crystal that is highly accurate in single slip and is also reasonably accurate in multiple slips. In this paper, we present a stress-point integration algorithm for crystal plasticity in the finite deformation range that is exact in single slip and highly accurate in multiple slips.

A first step in the development of an exact stress-point integration algorithm for crystals deforming in single slip is to reformulate the kinematics of crystalline slips as a strong discontinuity problem. Originally used to describe the kinematics of a shear band, and whether it is used in the context of the assumed enhanced strain or the extended finite element method, strong discontinuity is defined as the limit of weak discontinuity as the thickness of the band approaches zero [3,12,14,15,24,29,38,40–42,47,52,56]. We view the crystallographic planes in the same way as we view a shear band: it is a strong discontinuity where the strain rate is represented by a distribution (Dirac delta) function. For the yield stress to remain bounded, the plastic modulus must have

the form of an inverse of the distribution function so that the product of the strain rate and the plastic modulus (which describes the rate of change in the yield stress) remains bounded. The similarity of the shear band and crystal plasticity problems is not restricted to the strain singularity on the slip plane. In the shear band problem, the material outside the band typically undergoes elastic unloading as the band continues to yield plastically. In crystal plasticity, the lattice hosting the slip planes typically deforms elastically (unless it develops its own microstructure) while plastic slips take place on the glide planes.

In the formulation that follows, we use the strong discontinuity framework presented by Borja [13] for a shear band undergoing finite deformation. In this formulation, which we apply to the crystal plasticity problem, a strong discontinuity is embedded in an elastic deformable solid, which we now take to be the crystal lattice. An essential ingredient of the formulation is the multiscale framework that permits the decomposition of crystal deformation into a fine-scale field and a coarse-scale field. We introduce so-called continuous and conforming deformation fields that represent, respectively, the deformation of the crystal lattice and the overall macroscopic deformation of the crystal. From this formulation, we develop a stress-point integration algorithm that is exact for a crystal deforming in single slip, and is demonstrably accurate for a crystal deforming in multiple slips.

2. The fine-scale field

Consider a crystal lattice with one active slip system. Let $\boldsymbol{N}$ denote the unit normal to the glide plane in the reference configuration. We view this glide plane as a thin interface $\mathcal{D}_0$ with thickness h_0 in the reference configuration, and thickness h in the current configuration. By letting h_0 and h approach zero, we recover the strong discontinuity limit. The schematic of the problem is shown in Fig. 1.

2.1. Kinematics for single-slip

The kinematics for single slip in the finite deformation range follows the strong discontinuity framework presented in [13]. The intent of this section is not to be repetitive, but rather, to highlight the change in scale at which the strong discontinuity concept is used for the crystal problem. In particular, we distinguish between slip in the macro-mechanical framework of the previous paper and slip in the grain-scale framework proposed in the present paper. Keeping in mind that the kinematical descriptions are now local to the crystal, and thus, all spatial variations pertain to the crystal grain scale and not to the macroscopic scale, we write the local deformation in the crystal in the form

$$\phi = \begin{cases} \overline{\phi}, & \text{if } \kappa \leqslant 0; \\ \overline{\phi} + \kappa[\![\phi]\!]/h_0, & \text{if } 0 \leqslant \kappa \leqslant h_0; \\ \overline{\phi} + [\![\phi]\!], & \text{if } \kappa \geqslant h_0. \end{cases} \tag{1}$$

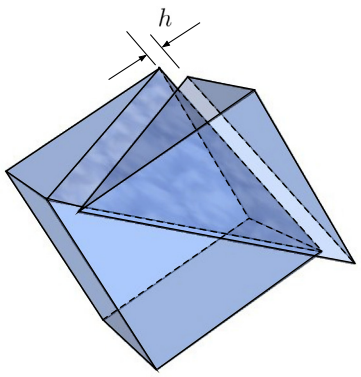

Fig. 1. Crystal lattice with one active slip system: the glide plane is assumed to be an interface with thickness h in the current configuration. Strong discontinuity is defined by the limit $h \to 0$.

We identify $\overline{\phi}$ as the deformation of the lattice in the neighborhood of $\mathcal{D}_0$, and $[\![\phi]\!]$ as the deformation of "face 2" relative to "face 1" of $\mathcal{D}_0$ (the choice of either face is arbitrary). The variable κ is a normal parameter given by the expression

$$\kappa = (\boldsymbol{X} - \boldsymbol{Y}) \cdot \boldsymbol{N}, \tag{2}$$

where $\boldsymbol{Y}$ is any point on face 1, whose unit normal is $\boldsymbol{N}$ and pointing in the direction of face 2. The corresponding deformation gradient is

$$\boldsymbol{F} = \frac{\partial \phi}{\partial \boldsymbol{X}} = \begin{cases} \boldsymbol{F}^{\mathrm{e}} & \text{outside } \mathcal{D}_0; \\ \boldsymbol{F}^{\mathrm{e}} + ([\![\phi]\!] \otimes \boldsymbol{N})/h_0 & \text{inside } \mathcal{D}_0, \end{cases} \tag{3}$$

where $\boldsymbol{F}^{\mathrm{e}} = \partial \overline{\phi}/\partial \boldsymbol{X}$. The superscript "e" in $\boldsymbol{F}^{\mathrm{e}}$ stands for 'elastic' and implies that the host lattice is deforming elastically whereas the interface volume $\mathcal{D}_0$ is deforming plastically. At this point we shall not rule out the possibility that the slip in $\mathcal{D}_0$ may also contain some elastic parts, although later we shall show that this is not true and that the slip in $\mathcal{D}_0$ is in fact completely inelastic. In the expressions above, we assume that $[\![\phi]\!]$ is locally constant within the lattice. The macroscopic counterpart of the above kinematical description is a tabular deformation band [10,11].

The velocity field in the crystal takes similar forms,

$$\boldsymbol{V} = \begin{cases} \overline{\boldsymbol{V}}, & \text{if } \kappa \leqslant 0; \\ \overline{\boldsymbol{V}} + \kappa [\![\boldsymbol{V}]\!]/h_0, & \text{if } 0 \leqslant \kappa \leqslant h_0; \\ \overline{\boldsymbol{V}} + [\![\boldsymbol{V}]\!], & \text{if } \kappa \geqslant h_0, \end{cases} \tag{4}$$

where $\overline{\boldsymbol{V}} = \dot{\overline{\phi}}$ and $[\![\boldsymbol{V}]\!] = [\![\dot{\phi}]\!]$. We recall that the velocity $\boldsymbol{V}(\boldsymbol{X})$ of material point X initially at position $\boldsymbol{X}$ is the same as the velocity $\boldsymbol{v}(\boldsymbol{x})$ of the same material point that is now at $\boldsymbol{x}$. The time derivative of $\boldsymbol{F}$ also takes similar forms

$$\dot{\boldsymbol{F}} = \begin{cases} \dot{\boldsymbol{F}}^{\mathrm{e}} & \text{outside } \mathcal{D}_0; \\ \dot{\boldsymbol{F}}^{\mathrm{e}} + ([\![\boldsymbol{V}]\!] \otimes \boldsymbol{N})/h_0 & \text{inside } \mathcal{D}_0, \end{cases} \tag{5}$$

where $\dot{\boldsymbol{F}} = \partial \boldsymbol{V}/\partial \boldsymbol{X}$ and $\dot{\boldsymbol{F}}^{\mathrm{e}} = \partial \overline{\boldsymbol{V}}/\partial \boldsymbol{X}$. The Sherman–Morrison formula provides the inverse of $\boldsymbol{F}$,

$$\boldsymbol{F}^{-1} = \begin{cases} \boldsymbol{F}^{\mathrm{e}-1} & \text{outside } \mathcal{D}_0; \\ \boldsymbol{F}^{\mathrm{e}-1} - (\boldsymbol{\Phi} \otimes \boldsymbol{N} \cdot \boldsymbol{F}^{\mathrm{e}-1})/(h_0 + \boldsymbol{N} \cdot \boldsymbol{\Phi}) & \text{inside } \mathcal{D}_0, \end{cases} \tag{6}$$

where $\boldsymbol{\Phi} = \boldsymbol{F}^{\mathrm{e}-1} \cdot [\![\phi]\!]$ is the elastic pull-back of $[\![\phi]\!]$. Now, consider an infinitesimal volume $\mathrm{d}V = h_0 \mathrm{d}A$ in the reference configuration, where $\mathrm{d}A$ is an infinitesimal area on the plane of the interface $\mathcal{D}_0$. Upon deformation, $\mathrm{d}V$ becomes $\mathrm{d}v = h\mathrm{d}a$, where h is the thickness of the interface in the current configuration and $\mathrm{d}a$ is the deformed area. Nanson's formula states that $\boldsymbol{n}\mathrm{d}a = J\boldsymbol{N} \cdot \boldsymbol{F}^{-1}\mathrm{d}A$ [43], where $J = \mathrm{d}v/\mathrm{d}V$ and $\boldsymbol{n}$ is a unit vector normal to the deformed area. This gives

$$\frac{\boldsymbol{n}}{h} = \frac{\boldsymbol{N} \cdot \boldsymbol{F}^{-1}}{h_0} = \frac{\boldsymbol{N} \cdot \boldsymbol{F}^{\mathrm{e}-1}}{h_0 + \boldsymbol{N} \cdot \boldsymbol{\Phi}}. \tag{7}$$

From the above equation, we obtain the evolution of the interface thickness of the form

$$h = h_0 \boldsymbol{n} \cdot \boldsymbol{F}^{\mathrm{e}} \cdot \boldsymbol{N} + \boldsymbol{n} \cdot [\![\phi]\!]. \tag{8}$$

The first term on the right-hand side is the elastic stretch in the direction of the thickness, while the second term is the stretch arising from the relative movement of the opposite faces of the interface. In the strong discontinuity limit, both h_0 and h must approach zero, which means that $\boldsymbol{n}$ must be perpendicular to $[\![\phi]\!]$. Using the identity $\boldsymbol{l} = \dot{\boldsymbol{F}} \cdot \boldsymbol{F}^{-1}$ for the velocity gradient, we obtain

$$\boldsymbol{l} = \begin{cases} \boldsymbol{l}^{\mathrm{e}} & \text{outside } \mathcal{D}_0; \\ \\ \boldsymbol{l}^{\mathrm{e}} + (\overset{\nabla}{[\![\phi]\!]} \otimes \boldsymbol{n})/h & \text{inside } \mathcal{D}_0, \end{cases} \tag{9}$$

where

$$\boldsymbol{l}^{\mathrm{e}} = \dot{\boldsymbol{F}}^{\mathrm{e}} \cdot \boldsymbol{F}^{\mathrm{e}-1}, \quad \overset{\triangledown}{[\![\phi]\!]} = [\![\dot{\phi}]\!] - \boldsymbol{l}^{\mathrm{e}} \cdot [\![\phi]\!]. \tag{10}$$

Note that $\overset{\triangledown}{[\![\phi]\!]}$ contains a convected part, which makes it an objective rate co-rotational with $[\![\phi]\!]$.

Theory of distribution may be used as a passage to the strong discontinuity limit. We recall that $\boldsymbol{n} \perp [\![\phi]\!]$ in the limit, where $\boldsymbol{n}$ is an $\boldsymbol{F}^{\mathrm{e}}$-covariant transformation of $\boldsymbol{N}$. Therefore, $[\![\phi]\!]$ must be an $\boldsymbol{F}^{\mathrm{e}}$-contravariant transformation of some unit tangent vector $\boldsymbol{M} \perp \boldsymbol{N}$ in the reference configuration. The two unit vectors $\boldsymbol{M}$ and $\boldsymbol{N}$ define the primary slip system in the reference configuration. Therefore, the displacement jump in the current configuration can be written as

$$[\![\phi]\!] := \gamma \boldsymbol{F}^{\mathrm{e}} \cdot \boldsymbol{M}, \tag{11}$$

where γ is the cumulative slip in the reference configuration. After noting that $\boldsymbol{M}$ is fixed and $\dot{\boldsymbol{F}}^{\mathrm{e}} = \boldsymbol{l}^{\mathrm{e}} \cdot \boldsymbol{F}^{\mathrm{e}}$, we obtain the rate form

$$[\![\dot{\phi}]\!] = \dot{\gamma} \boldsymbol{F}^{\mathrm{e}} \cdot \boldsymbol{M} + \gamma \dot{\boldsymbol{F}}^{\mathrm{e}} \cdot \boldsymbol{M} = \dot{g} \boldsymbol{m} + \boldsymbol{l}^{\mathrm{e}} \cdot [\![\phi]\!], \tag{12}$$

where

$$\boldsymbol{m} = \boldsymbol{F}^{\mathrm{e}} \cdot \boldsymbol{M} / \| \boldsymbol{F}^{\mathrm{e}} \cdot \boldsymbol{M} \| \tag{13}$$

is the unit vector in the direction of slip, and $\dot{g} = \dot{\gamma} \| \boldsymbol{F}^{\mathrm{e}} \cdot \boldsymbol{M} \|$ is the slip rate in the current configuration. This simplifies the co-rotational jump rate to the form

$$\overset{\triangledown}{[\![\phi]\!]} = \dot{g} \boldsymbol{m}. \tag{14}$$

Denoting the distribution function by the symbol $\delta_{\mathcal{D}}$ (the Dirac delta function), we write the rate of deformation gradient 'inside' $\mathcal{D}_0$ as the sum of a regular part and a singular part,

$$\dot{\boldsymbol{F}} = \dot{\boldsymbol{F}}^{\mathrm{e}} + \delta_{\mathcal{D}} ([\![\dot{\phi}]\!] \otimes \boldsymbol{N}). \tag{15}$$

The regular part is the elastic rate of deformation gradient in the neighborhood of the slip plane, whereas the singular part is the slip on this plane. Similarly, the velocity gradient 'inside' the glide plane can be decomposed additively into regular and singular parts,

$$\boldsymbol{l} = \boldsymbol{l}^{\mathrm{e}} + \delta_{\mathcal{D}} (\dot{g} \boldsymbol{m} \otimes \boldsymbol{n}). \tag{16}$$

The above equations are useful mathematical representations for the constitutive formulation described in the next section.

2.2. Constitutive formulation

The underlying constitutive framework for the proposed crystal plasticity theory relies on the notion of multiplicative decomposition of deformation gradient into elastic and plastic parts, i.e., $\boldsymbol{F} = \boldsymbol{F}^{\mathrm{e}} \cdot \boldsymbol{F}^{\mathrm{p}}$. Crystal elasticity can be very complex, see [2,27,35,61,62], for example. Less symmetric crystals require more elastic constants and far more elaborate stored energy functions in the finite deformation range. Recognizing that the deformations considered in the present paper are dominated by inelastic slips, and that elastic deformations are small in comparison to these slips, we consider isotropic elasticity for simplicity in the formulation and write the stored energy function as $\Psi = \Psi(\boldsymbol{b}^{\mathrm{e}})$, where $\boldsymbol{b}^{\mathrm{e}}$ is the elastic left Cauchy–Green deformation tensor defined as

$$\boldsymbol{b}^{\mathrm{e}} = \boldsymbol{F}^{\mathrm{e}} \cdot \boldsymbol{F}^{\mathrm{e}\mathsf{T}} = \boldsymbol{F} \cdot \boldsymbol{C}^{\mathrm{p}-1} \cdot \boldsymbol{F}^{\mathsf{T}} \tag{17}$$

and $\boldsymbol{C}^{\mathrm{p}} = \boldsymbol{F}^{\mathrm{p}\mathsf{T}} \cdot \boldsymbol{F}^{\mathrm{p}}$ is the plastic right Cauchy–Green deformation tensor. The assumption of elastic isotropy also permits the symmetric Kirchhoff stress tensor to be written in the form

$$\boldsymbol{\tau} = 2 \frac{\partial \Psi}{\partial \boldsymbol{b}^{\mathrm{e}}} \cdot \boldsymbol{b}^{\mathrm{e}} = 2 \boldsymbol{b}^{\mathrm{e}} \cdot \frac{\partial \Psi}{\partial \boldsymbol{b}^{\mathrm{e}}}, \tag{18}$$

i.e., $\partial \Psi / \partial \boldsymbol{b}^{\mathrm{e}}$ and $\boldsymbol{b}^{\mathrm{e}}$ commute.

Taking the time derivative of the Kirchhoff stress gives the elastic rate constitutive equation

$$\dot{\boldsymbol{\tau}} = \frac{1}{2}\boldsymbol{\varphi}^{\mathrm{e}} : \dot{\boldsymbol{b}}^{\mathrm{e}} = \frac{1}{2}\boldsymbol{\varphi}^{\mathrm{e}} : (\boldsymbol{l}^{\mathrm{e}} \cdot \boldsymbol{b}^{\mathrm{e}} + \boldsymbol{b}^{\mathrm{e}} \cdot \boldsymbol{l}^{\mathrm{e}\mathsf{T}}) = \boldsymbol{\alpha}^{\mathrm{e}} : \boldsymbol{l}^{\mathrm{e}}, \tag{19}$$

where $\boldsymbol{\varphi}^{\mathrm{e}} = 2\partial\boldsymbol{\tau}/\partial\boldsymbol{b}^{\mathrm{e}}$ and $\boldsymbol{\alpha}^{\mathrm{e}} = \boldsymbol{\varphi}^{\mathrm{e}} \cdot \boldsymbol{b}^{\mathrm{e}}$. We recall the spectral representation of the spatial elasticity tensor $\boldsymbol{\alpha}^{\mathrm{e}}$ developed in [12,13,49],

$$\boldsymbol{\alpha}^{\mathrm{e}} = \sum_{A=1}^{3}\sum_{B=1}^{3} a^{\mathrm{e}}_{AB}\boldsymbol{m}^{(A)} \otimes \boldsymbol{m}^{(B)} + \sum_{A=1}^{3}\sum_{B\neq A}\left(\frac{\tau_B - \tau_A}{\overline{\lambda}^{\mathrm{e}}_B - \overline{\lambda}^{\mathrm{e}}_A}\right)(\overline{\lambda}^{\mathrm{e}}_B \boldsymbol{m}^{(AB)} \otimes \boldsymbol{m}^{(AB)} + \overline{\lambda}^{\mathrm{e}}_A \boldsymbol{m}^{(AB)} \otimes \boldsymbol{m}^{(BA)}), \tag{20}$$

where τ_A and $\overline{\lambda}^{\mathrm{e}}_A$ are principal values of $\boldsymbol{\tau}$ and $\boldsymbol{b}^{\mathrm{e}}$, respectively, $\boldsymbol{m}^{(AB)} = \boldsymbol{n}^{(A)} \otimes \boldsymbol{n}^{(B)}$ are spectral directions constructed from the principal directions $\boldsymbol{n}^{(A)}$ of $\boldsymbol{\tau}$ (or from the principal directions of $\boldsymbol{b}^{\mathrm{e}}$ by coaxiality), and a^{e}_{AB} is the matrix of elastic moduli in principal axes, given in terms of the elastic bulk modulus K and elastic shear modulus μ by [55,57]

$$[a^{\mathrm{e}}_{AB}] = \begin{bmatrix} a & b & b \\ b & a & b \\ b & b & a \end{bmatrix}, \quad a = K + \frac{4}{3}\mu, \quad b = K - \frac{2}{3}\mu. \tag{21}$$

If $\boldsymbol{P}$ denotes the first Piola–Kirchhoff stress tensor and $\mathbf{A}^{\mathrm{e}} = \partial\boldsymbol{P}/\partial\boldsymbol{F}^{\mathrm{e}}$ denotes the two-point elasticity tensor with components $\mathsf{A}^{\mathrm{e}}_{iAjB} = \partial P_{iA}/\partial F^{\mathrm{e}}_{jB}$, then the spatial elasticity tensor is

$$\boldsymbol{\alpha}^{\mathrm{e}} = \mathbf{a}^{\mathrm{e}} + \boldsymbol{\tau} \ominus \mathbf{1}, \tag{22}$$

where the components are $\mathsf{a}^{\mathrm{e}}_{ikjl} = F_{kA}F_{lB}\mathsf{A}^{\mathrm{e}}_{iAjB}$ and $(\boldsymbol{\tau} \ominus \mathbf{1})_{ijkl} = \tau_{il}\delta_{jk}$.

The additive decomposition of the spatial velocity gradient shown in (16) identifies the plastic component of the velocity gradient as

$$\boldsymbol{l}^{\mathrm{p}} = \delta_{\mathcal{D}}(\dot{g}\boldsymbol{m} \otimes \boldsymbol{n}). \tag{23}$$

Note that this plastic component is singular as a result of the strong discontinuity assumption. In addition, from the relation $\boldsymbol{l}^{\mathrm{e}} = \dot{\boldsymbol{F}}^{\mathrm{e}} \cdot \boldsymbol{F}^{\mathrm{e}-1}$, and from the expansion

$$\boldsymbol{l} = \dot{\boldsymbol{F}}^{\mathrm{e}} \cdot \boldsymbol{F}^{\mathrm{e}-1} + \boldsymbol{F}^{\mathrm{e}} \cdot (\dot{\boldsymbol{F}}^{\mathrm{p}} \cdot \boldsymbol{F}^{\mathrm{p}-1}) \cdot \boldsymbol{F}^{\mathrm{e}-1}, \tag{24}$$

we find that

$$\dot{\boldsymbol{F}}^{\mathrm{p}} \cdot \boldsymbol{F}^{\mathrm{p}-1} = \delta_{\mathcal{D}}(\boldsymbol{F}^{\mathrm{e}-1} \cdot \dot{g}\boldsymbol{m}) \otimes (\boldsymbol{n} \cdot \boldsymbol{F}^{\mathrm{e}}), \tag{25}$$

which has a form similar to the one proposed by Rice [53]. We readily see from the above development that the slip rate is fully plastic, i.e., it has no elastic part.

Eq. (23) suggests that the plastic flow direction is $\boldsymbol{m} \otimes \boldsymbol{n}$ (i.e., the Schmid tensor) and that the consistency parameter is the delta function $\delta_{\mathcal{D}}$ with a regular multiplier $\dot{g}$. If one derives the plastic flow direction from a plastic potential function, then an associated plastic flow implies that this plastic potential function must be the same as the yield function

$$\mathcal{F} = |(\boldsymbol{m} \otimes \boldsymbol{n}) : \boldsymbol{\tau}| - \tau_Y \equiv \psi(\boldsymbol{m} \otimes \boldsymbol{n}) : \boldsymbol{\tau} - \tau_Y \leqslant 0, \tag{26}$$

where

$$\psi := \mathrm{sign}((\boldsymbol{m} \otimes \boldsymbol{n}) : \boldsymbol{\tau}) \tag{27}$$

is the sign function and τ_Y is the yield stress on the slip system. Furthermore, the plastic component of velocity gradient has singular symmetric and skew-symmetric parts,

$$\boldsymbol{d}^{\mathrm{p}} = \delta_{\mathcal{D}}\psi\,\mathrm{sym}(\dot{g}\boldsymbol{m} \otimes \boldsymbol{n}), \quad \boldsymbol{\omega}^{\mathrm{p}} = \delta_{\mathcal{D}}\psi\,\mathrm{skw}(\dot{g}\boldsymbol{m} \otimes \boldsymbol{n}). \tag{28}$$

Note that the presence of the sign function ensures that only forward slips are considered. Since $\boldsymbol{m}, \boldsymbol{n}$, and $\boldsymbol{\tau}$ all depend on the elastic deformation gradient $\boldsymbol{F}^{\mathrm{e}}$, the consistency condition on the yield function writes

$$\dot{\mathcal{F}} = \frac{\partial \mathcal{F}}{\partial \boldsymbol{F}^{\mathrm{e}}} : \dot{\boldsymbol{F}}^{\mathrm{e}} - \delta_{\mathcal{D}} \dot{g} H = 0, \tag{29}$$

where H is the generalized plastic modulus. The first term on the right is a regular function, whereas the second term is singular – unless H is of the form

$$H = \mathcal{H}_{\mathcal{D}} / \delta_{\mathcal{D}}, \tag{30}$$

where $\mathcal{H}_{\mathcal{D}}$ is a regular function. If this is the case, then the consistency condition becomes

$$\dot{\mathcal{F}} = \frac{\partial \mathcal{F}}{\partial \boldsymbol{F}^{\mathrm{e}}} : \dot{\boldsymbol{F}}^{\mathrm{e}} - \dot{g} \mathcal{H}_{\mathcal{D}} = 0. \tag{31}$$

Note that all terms in the above equation are now regular functions.

The strong discontinuity theory can be fully appreciated from the regularized formulation. Take $h > 0$, for example. The regularized form of the plastic component of velocity gradient is then given by $\boldsymbol{l}^{\mathrm{p}} = (\dot{g} \boldsymbol{m} \otimes \boldsymbol{n})/h$. As h tends to zero, $\dot{g}/h$ becomes very large (i.e., unbounded) due to plastic strain localization on the glide plane. However, the consistency condition cannot contain unbounded terms, so the plastic modulus must necessarily be of the form $H = \mathcal{H}_{\mathcal{D}} h$, i.e., it must be $\mathrm{O}(h)$. This means that as h approaches zero the plastic modulus must approach zero in order for the yield stress to remain bounded. This corresponds to perfect plasticity in the continuum sense. However, it can be seen from the above formulation that the singular terms cancel out, leaving only the regular terms, thus allowing the yield stress τ_Y to increase or decrease with plastic deformation in a regular fashion (depending on the sign of $\mathcal{H}_{\mathcal{D}}$) even in the limit when the continuum plastic modulus is zero.

3. The coarse-scale field

So far, the kinematical descriptions discussed have focused on the fine-scale deformation field in the neighborhood of the slip systems. Of interest, however, is the overall response of a crystal represented by the combined elastic lattice deformation and inelastic slips on the glide planes. This corresponds to the coarse-scale field; the associated coarse-scale deformation is then a smoothed version of the fine-scale deformations.

3.1. Multiscale kinematics

As an illustration of the interplay between the coarse- and fine-scale fields, consider the following fine-scale displacement field in the neighborhood of a primary slip system (see Figs. 2 and 3):

$$\boldsymbol{u}(\boldsymbol{X}) = \overline{\boldsymbol{u}}(\boldsymbol{X}) + [\![\boldsymbol{u}(\boldsymbol{X})]\!] H_{\mathcal{D}}(\boldsymbol{X}), \quad H_{\mathcal{D}}(\boldsymbol{X}) = \begin{cases} 1 & \text{if } \boldsymbol{X} \in \mathcal{D}_+ \\ 0 & \text{if } \boldsymbol{X} \in \mathcal{D}_- \end{cases}, \tag{32}$$

where $\mathcal{D}_\pm$ represents regions in the crystal lattice on the opposite sides of the glide plane (the choice of $+$ and $-$ sides is arbitrary). Note that we have used the Heaviside function in lieu of the ramp function to define the limiting condition of strong discontinuity. The displacement field $\overline{\boldsymbol{u}}$ is the continuous part of $\boldsymbol{u}$ and delineates the elastic deformation of the crystal lattice, whereas $[\![\boldsymbol{u}]\!]$ is the slip on the primary system given more specifically by

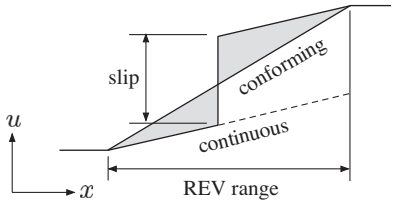

Fig. 2. One-dimensional representation of continuous and conforming displacement fields: the conforming displacement field is a smoothed overall displacement of the crystal taken over the representative elementary volume (REV) range; the continuous field defines the elastic deformation of the crystal lattice.

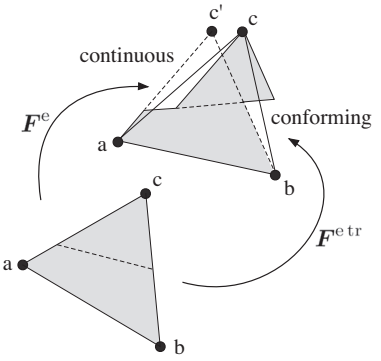

Fig. 3. Two-dimensional representation of continuous and conforming deformation fields: shaded region is crystal lattice in the reference (bottom) and current (top) configurations. For single-slip systems, $\boldsymbol{F}^{e\,tr}$ induces the same rotation on the crystal lattice as $\boldsymbol{F}^e$.

$$[\![\boldsymbol{u}(\boldsymbol{X})]\!] = \zeta(\boldsymbol{X})\boldsymbol{m}(\boldsymbol{X}) = \zeta \boldsymbol{F}^e \cdot \boldsymbol{M} / \|\boldsymbol{F}^e \cdot \boldsymbol{M}\|, \tag{33}$$

where

$$\zeta = \gamma \|\boldsymbol{F}^e \cdot \boldsymbol{M}\| \tag{34}$$

is the cumulative slip measured with respect to the reference configuration, cf. Eq. (11). Note that $[\![\boldsymbol{u}]\!]$ is always co-rotational with the glide plane.

The coarse-scale displacement is a conforming field that is macroscopically smooth. In finite element analysis, for example, the conforming field is the continuous spatial displacement field provided by the standard finite element interpolation. We can re-parameterize the same 'true' displacement field $\boldsymbol{u}$ in the form

$$\boldsymbol{u}(\boldsymbol{X}) = \widetilde{\boldsymbol{u}}(\boldsymbol{X}) + [\![\boldsymbol{u}(\boldsymbol{X})]\!] M_{\mathcal{D}}(\boldsymbol{X}), \tag{35}$$

where $\widetilde{\boldsymbol{u}}$ is the coarse-scale displacement field, and

$$M_{\mathcal{D}} = H_{\mathcal{D}}(\boldsymbol{X}) - G(\boldsymbol{X}), \tag{36}$$

delineates the variation of the fine-scale field. In the above equation, $G(\boldsymbol{X})$ is an arbitrary smooth ramp function that varies from zero to one over a unit thickness in the direction of $\boldsymbol{N}$. We remark that $G(\boldsymbol{X})$ does not serve as an approximation to the Heaviside function, but rather, it merely defines the range over which the displacement jump is being smoothed over by the conforming displacement field. As shown subsequently, this range is immaterial to the formulation since we will only be dealing with the deformation gradients in subsequent discussions. We thus view the displacement field $\boldsymbol{u}$ as being the sum of the coarse-scale field $\widetilde{\boldsymbol{u}}$ and the fine-scale field $[\![\boldsymbol{u}]\!] M_{\mathcal{D}}$, where the latter function is represented by the shaded region in Fig. 2.

Since the displacement jump $[\![\boldsymbol{u}]\!]$ is assumed to be spatially constant within the domain on the $\mathcal{D}_+$ side of the crystal, we can define the continuous deformation in the crystal lattice as the total deformation minus the deformation jump, i.e.,

$$\overline{\boldsymbol{x}} = \boldsymbol{X} + \overline{\boldsymbol{u}}. \tag{37}$$

The continuous deformation field delineates the elastic deformation of the lattice. On the other hand, the conforming deformation field delineates the overall (smoothed) deformation of the crystal,

$$\widetilde{\boldsymbol{x}} = \boldsymbol{X} + \widetilde{\boldsymbol{u}}. \tag{38}$$

The continuous and conforming deformations are related by the equation

$$\overline{\boldsymbol{x}} = \widetilde{\boldsymbol{x}} - [\![\boldsymbol{u}]\!] G(\boldsymbol{X}). \tag{39}$$

Letting $\boldsymbol{F}^e = \partial \overline{\boldsymbol{x}} / \partial \boldsymbol{X}$ and $\boldsymbol{F}^{e\,tr} = \partial \widetilde{\boldsymbol{x}} / \partial \boldsymbol{X}$, we have

$$\boldsymbol{F}^e = \boldsymbol{F}^{e\,tr} - \zeta \boldsymbol{m} \otimes \frac{\partial G}{\partial \boldsymbol{X}} = \boldsymbol{F}^{e\,tr} - \zeta \boldsymbol{m} \otimes \boldsymbol{N}. \tag{40}$$

Note that the same symbol ζ is used to denote a measure of slip per unit distance over which the slip is being smoothed over (a slight abuse in notation). This makes ζ a dimensionless quantity, and its numerical value expressible in percent (as in strain). Imposing the above equation at time t_n readily gives

$$\boldsymbol{F}^{\mathrm{e}}_n = \boldsymbol{F}^{\mathrm{e\ tr}}_n - \zeta_n \boldsymbol{m}_n \otimes \frac{\partial G}{\partial \boldsymbol{X}} = \boldsymbol{F}^{\mathrm{e\ tr}}_n - \zeta_n \boldsymbol{m}_n \otimes \boldsymbol{N}, \tag{41}$$

where $\boldsymbol{F}^{\mathrm{e}}_n = \partial \overline{\boldsymbol{x}}_n / \partial \boldsymbol{X}$ and $\boldsymbol{F}^{\mathrm{e\ tr}}_n = \partial \widetilde{\boldsymbol{x}}_n / \partial \boldsymbol{X}$. The superscript "e" suggests an elastic deformation field in the lattice defined by the continuous deformation field, whereas the superscript "e tr" suggests a trial elastic predictor that would be the true deformation field if we did not allow any plastic slip to occur in the crystal. We shall refer to the latter as the coarse-scale deformation gradient, i.e., the deformation gradient for the crystal as a whole.

The discrete formulation aims to time-integrate the stress and deformation variables over discrete time intervals. Taking the configuration at t_n as the reference configuration, the relative deformation gradients at any time $t > t_n$ can be written as

$$\boldsymbol{f}^{\mathrm{e}} = \frac{\partial \overline{\boldsymbol{x}}}{\partial \overline{\boldsymbol{x}}_n} = \boldsymbol{F}^{\mathrm{e}} \cdot \boldsymbol{F}^{\mathrm{e}-1}_n, \quad \boldsymbol{f}^{\mathrm{e\ tr}} = \frac{\partial \widetilde{\boldsymbol{x}}}{\partial \widetilde{\boldsymbol{x}}_n} = \boldsymbol{F}^{\mathrm{e\ tr}} \cdot \boldsymbol{F}^{\mathrm{e\ tr}-1}_n. \tag{42}$$

The term $\boldsymbol{f}^{\mathrm{e\ tr}}$ in the above expression is the coarse-scale relative deformation gradient. We can use the Sherman-Morrison formula to find the inverses

$$\boldsymbol{F}^{\mathrm{e}-1} = \boldsymbol{F}^{\mathrm{e\ tr}-1} + \frac{\zeta}{1-\zeta\beta} \boldsymbol{F}^{\mathrm{e\ tr}-1} \cdot \boldsymbol{m} \otimes \boldsymbol{N} \cdot \boldsymbol{F}^{\mathrm{e\ tr}-1} \tag{43}$$

and

$$\boldsymbol{F}^{\mathrm{e}-1}_n = \boldsymbol{F}^{\mathrm{e\ tr}-1}_n + \frac{\zeta_n}{1-\zeta_n\beta_n} \boldsymbol{F}^{\mathrm{e\ tr}-1}_n \cdot \boldsymbol{m}_n \otimes \boldsymbol{N} \cdot \boldsymbol{F}^{\mathrm{e\ tr}-1}_n, \tag{44}$$

where $\beta = \boldsymbol{N} \cdot \boldsymbol{F}^{\mathrm{e\ tr}-1} \cdot \boldsymbol{m}$ and $\beta_n = \boldsymbol{N} \cdot \boldsymbol{F}^{\mathrm{e\ tr}-1}_n \cdot \boldsymbol{m}_n$. From Eq. (42), we find

$$\boldsymbol{f}^{\mathrm{e}} = \boldsymbol{f}^{\mathrm{e\ tr}} - \overset{\triangledown}{\boldsymbol{m}} \otimes \boldsymbol{N} \cdot \boldsymbol{F}^{\mathrm{e\ tr}-1}_n, \tag{45}$$

where

$$\overset{\triangledown}{\boldsymbol{m}} = \frac{\zeta}{1-\zeta_n\beta_n} \boldsymbol{m} - \frac{\zeta_n}{1-\zeta_n\beta_n} \boldsymbol{f}^{\mathrm{e\ tr}} \cdot \boldsymbol{m}_n \tag{46}$$

is the incremental slip over the relevant time interval. For future use, we also present the inverse of $\boldsymbol{f}^{\mathrm{e}}$ as

$$\boldsymbol{f}^{\mathrm{e}-1} = \boldsymbol{f}^{\mathrm{e\ tr}-1} + \overset{\triangledown}{\boldsymbol{m}}_n \otimes \boldsymbol{N} \cdot \boldsymbol{F}^{\mathrm{e\ tr}-1}, \tag{47}$$

where

$$\overset{\triangledown}{\boldsymbol{m}}_n = \frac{\zeta}{1-\zeta\beta} \boldsymbol{f}^{\mathrm{e\ tr}-1} \cdot \boldsymbol{m} - \frac{\zeta_n}{1-\zeta\beta} \boldsymbol{m}_n. \tag{48}$$

The above formulation shows that the elastic deformation gradients $\boldsymbol{F}^{\mathrm{e}}$ and $\boldsymbol{f}^{\mathrm{e}}$ are functions of the current slip direction $\boldsymbol{m}$, which in turn is a function of the elastic deformation gradient $\boldsymbol{F}^{\mathrm{e}}$. This elliptic relation would be difficult to solve analytically for $\boldsymbol{f}^{\mathrm{e}}$, unless we recognize the strain-driven format of the algorithm and the role played by the coarse-scale displacement field in the algorithmic formulation. In a strain-driven format, we are given the elastic left Cauchy-Green deformation tensor $\boldsymbol{b}^{\mathrm{e}}_n$ at time t_n, as well as the coarse-scale displacement increment $\Delta\widetilde{\boldsymbol{u}} = \widetilde{\boldsymbol{u}} - \widetilde{\boldsymbol{u}}_n$; we then want to find the elastic left Cauchy-Green deformation tensor $\boldsymbol{b}^{\mathrm{e}}$ at any time $t > t_n$. The elastic predictors are defined by the coarse-scale deformation gradients themselves,

$$\boldsymbol{F}^{\mathrm{e\ tr}} = \boldsymbol{F}^{\mathrm{e\ tr}}_n + \frac{\partial \Delta\widetilde{\boldsymbol{u}}}{\partial \boldsymbol{X}}, \quad \boldsymbol{f}^{\mathrm{e\ tr}} = \boldsymbol{1} + \frac{\partial \Delta\widetilde{\boldsymbol{u}}}{\partial \widetilde{\boldsymbol{x}}_n}. \tag{49}$$

Now, the transformation for the slip direction $\boldsymbol{m}$ is given by Eq. (13), or, equivalently, by the relation

$$\boldsymbol{m} = \boldsymbol{f}^{\mathrm{e}} \cdot \boldsymbol{m}_n / \|\boldsymbol{f}^{\mathrm{e}} \cdot \boldsymbol{m}_n\|. \tag{50}$$

Therefore, we obtain

$$\boldsymbol{f}^{\mathrm{e}} \cdot \boldsymbol{m}_n = \|\boldsymbol{f}^{\mathrm{e}} \cdot \boldsymbol{m}_n\| \boldsymbol{m} = \frac{1}{1 - \zeta_n \beta_n} \boldsymbol{f}^{\mathrm{e\,tr}} \cdot \boldsymbol{m}_n - \frac{\zeta \beta_n}{1 - \zeta_n \beta_n} \boldsymbol{m}. \tag{51}$$

We see from the above relation that the vector formed by $\boldsymbol{f}^{\mathrm{e\,tr}} \cdot \boldsymbol{m}_n$ is parallel to the vector $\boldsymbol{m}$, and so we can use the alternative expression

$$\boldsymbol{m} = \boldsymbol{f}^{\mathrm{e\,tr}} \cdot \boldsymbol{m}_n / \|\boldsymbol{f}^{\mathrm{e\,tr}} \cdot \boldsymbol{m}_n\| = \boldsymbol{F}^{\mathrm{e\,tr}} \cdot \boldsymbol{M} / \|\boldsymbol{F}^{\mathrm{e\,tr}} \cdot \boldsymbol{M}\|. \tag{52}$$

Similarly, we have

$$\boldsymbol{m}_n = \boldsymbol{F}_n^{\mathrm{e\,tr}} \cdot \boldsymbol{M} / \|\boldsymbol{F}_n^{\mathrm{e\,tr}} \cdot \boldsymbol{M}\|. \tag{53}$$

Because the coarse-scale deformation gradient $\boldsymbol{F}^{\mathrm{e\,tr}}$ determines the new orientation of $\boldsymbol{M}$, it follows that $\beta, \beta_n \propto \boldsymbol{M} \cdot \boldsymbol{N} \equiv 0$, and so the update equation for $\boldsymbol{f}^{\mathrm{e}}$ simplifies to the form

$$\boldsymbol{f}^{\mathrm{e}} = \boldsymbol{f}^{\mathrm{e\,tr}} - \Delta\zeta \boldsymbol{m} \otimes \boldsymbol{N} \cdot \boldsymbol{F}_n^{\mathrm{e\,tr}-1}, \tag{54}$$

where

$$\Delta\zeta = \zeta - \zeta_n \|\boldsymbol{f}^{\mathrm{e\,tr}} \cdot \boldsymbol{m}_n\|. \tag{55}$$

The above developments suggest that for single-slip systems the rotation induced by the crystal lattice on the slip system is the same as the rotation induced by the crystal itself.

To elaborate the last sentence of the preceding paragraph, consider a rigid and non-rotating lattice for which the rotations of $\boldsymbol{M}$ and $\boldsymbol{N}$ are zero. Assuming a horizontal slip plane XY with slip occurring in the X-direction, then simple shearing on the scale of the crystal would produce grain-scale displacement fields $u_X = cZ$ and $u_Y = u_Z = 0$ on the representative elementary volume, where c is determined by slip in the X-direction. The continuum deformation gradient $\boldsymbol{F}$ then operates on $\boldsymbol{M} = \{1, 0, 0\}$ and $\boldsymbol{N} = \{0, 0, 1\}$ according to the relations $\boldsymbol{F} \cdot \boldsymbol{M} \equiv \boldsymbol{M}$ and $\boldsymbol{F}^{-\mathsf{T}} \cdot \boldsymbol{N} \equiv \boldsymbol{N}$. This means that the rotation of the slip tensor is zero even if the rotation of the crystal itself is not zero.

3.2. Stress-point integration

Direct time integration of the elastic left Cauchy–Green deformation tensor gives the update equation

$$\boldsymbol{b}^{\mathrm{e}}(t > t_n) = \boldsymbol{f}^{\mathrm{e}} \cdot \boldsymbol{b}_n^{\mathrm{e}} \cdot \boldsymbol{f}^{\mathrm{e}\mathsf{T}}. \tag{56}$$

The above expression is exact since time differentiation reverts back to the original rate equation

$$\dot{\boldsymbol{b}}^{\mathrm{e}} = \boldsymbol{l}^{\mathrm{e}} \cdot \boldsymbol{b}^{\mathrm{e}} + \boldsymbol{b}^{\mathrm{e}} \cdot \boldsymbol{l}^{\mathrm{e}\mathsf{T}}, \quad \boldsymbol{l}^{\mathrm{e}} = \dot{\boldsymbol{f}}^{\mathrm{e}} \cdot \boldsymbol{f}^{\mathrm{e}-1}. \tag{57}$$

This expression for $\boldsymbol{b}^{\mathrm{e}}$ is driven by the coarse-scale incremental displacement field $\Delta\widetilde{\boldsymbol{u}}$ alone, and so we can readily perform a spectral decomposition of $\boldsymbol{b}^{\mathrm{e}}$ as

$$\boldsymbol{b}^{\mathrm{e}} = \sum_{A=1}^{3} \lambda_A^2 \boldsymbol{n}^{(A)} \otimes \boldsymbol{n}^{(A)}, \tag{58}$$

where the λ_A^2's are the principal values of $\boldsymbol{b}^{\mathrm{e}}$ and the $\boldsymbol{n}^{(A)}$'s are the corresponding principal directions (not to be confused with the glide plane normal vector $\boldsymbol{n}$). The square roots of λ_A^2 are the elastic principal stretches, and $\varepsilon_A = \ln(\lambda_A)$ are the elastic logarithmic principal stretches. From the assumed isotropy in the elastic response, we can also decompose the symmetric Kirchhoff stress tensor spectrally as

$$\boldsymbol{\tau} = \sum_{A=1}^{3} \tau_A \boldsymbol{n}^{(A)} \otimes \boldsymbol{n}^{(A)}, \quad \tau_A = \frac{\partial \widehat{\Psi}}{\partial \epsilon_A}, \tag{59}$$

where $\widehat{\Psi} = \widehat{\Psi}(\varepsilon_1, \varepsilon_2, \varepsilon_3)$ is the same stored energy function introduced in Section 2.2 but is now expressed as a function of the elastic logarithmic principal stretches. A constraint on the Kirchhoff stress $\boldsymbol{\tau}$ is that it must satisfy the yield condition (26).

To summarize the stress-point integration algorithm for single-slip system, we rewrite the update equation for $\boldsymbol{f}^{\mathrm{e}}$ in a more general form as (cf. (54))

$$\boldsymbol{f}^{\mathrm{e}} = \boldsymbol{f}^{\mathrm{e\,tr}} - \Delta\zeta\psi\boldsymbol{m} \otimes \boldsymbol{N} \cdot \boldsymbol{F}_n^{\mathrm{e\,tr}-1}, \tag{60}$$

where the sign function has been introduced to ensure that $\psi\boldsymbol{m}$ always defines the direction of a forward slip. For a given $\Delta\zeta$ the right-hand side of the above equation is fully explicit, facilitating the sequence of calculations $\boldsymbol{f}^{\mathrm{e}} \to \boldsymbol{b}^{\mathrm{e}} \to \boldsymbol{\tau}$. In reality, $\Delta\zeta$ is unknown and must be iterated so as to satisfy the following discrete consistency condition

$$r(\Delta\zeta) = \psi(\boldsymbol{m} \otimes \boldsymbol{n}) : \boldsymbol{\tau} - (\tau_{Yn} + \Delta\zeta\mathcal{H}_{\mathcal{D}}) \to 0, \tag{61}$$

where $\mathcal{H}_{\mathcal{D}}$ is the (constant) plastic modulus, and τ_{Yn} is the resolved shear stress at the beginning of the load increment. In the above equation, we assume that the primary slip system is active at the beginning of the load increment, so that

$$\psi_n(\boldsymbol{m}_n \otimes \boldsymbol{n}_n) : \boldsymbol{\tau}_n - \tau_{Yn} = 0, \tag{62}$$

where ψ_n is the sign function evaluated at the beginning of the load increment, $\tau_{Yn} = \tau_{Y0} + \zeta_n\mathcal{H}_{\mathcal{D}}$, and τ_{Y0} is the initial yield stress.

Eq. (61) is a nonlinear equation in the slip increment $\Delta\zeta$ (see Eq. (55) for the explicit definition of this slip increment) that can be solved by a local Newton iteration. Note that $\boldsymbol{m}_n, \boldsymbol{n}_n$, and $\boldsymbol{\tau}_n$ are obtained from the previous load step, so they are fixed during the local iteration. Furthermore, the algorithm is driven by the coarse-scale displacement increment $\Delta\widetilde{\boldsymbol{u}}$, which is also fixed during the iteration. The local tangent operator then simplifies to the form

$$r'(\Delta\zeta) = \psi[(\boldsymbol{m} \otimes \boldsymbol{n}) : \boldsymbol{\tau}'(\Delta\zeta)] - \mathcal{H}_{\mathcal{D}}. \tag{63}$$

The derivative of $\boldsymbol{\tau}$ can be obtained from Eq. (19) as

$$\boldsymbol{\tau}'(\Delta\zeta) = \frac{1}{2}\boldsymbol{\varphi}^{\mathrm{e}} : \frac{\partial \boldsymbol{b}^{\mathrm{e}}}{\partial\Delta\zeta} = \boldsymbol{\alpha}^{\mathrm{e}} : \left(\frac{\partial \boldsymbol{f}^{\mathrm{e}}}{\partial\Delta\zeta} \cdot \boldsymbol{f}^{\mathrm{e}-1}\right). \tag{64}$$

We note that

$$\frac{\partial \boldsymbol{f}^{\mathrm{e}}}{\partial\Delta\zeta} = -\psi\boldsymbol{m} \otimes \boldsymbol{N} \cdot \boldsymbol{F}_n^{\mathrm{e\,tr}-1} \tag{65}$$

and

$$\frac{\partial \boldsymbol{f}^{\mathrm{e}}}{\partial\Delta\zeta} \cdot \boldsymbol{f}^{\mathrm{e}-1} = -\psi\boldsymbol{m} \otimes \boldsymbol{N} \cdot \boldsymbol{F}^{\mathrm{e\,tr}-1}. \tag{66}$$

So, the derivative of the Kirchhoff stress simplifies to

$$\boldsymbol{\tau}'(\Delta\zeta) = -\boldsymbol{\alpha}^{\mathrm{e}} : \left(\psi\boldsymbol{m} \otimes \boldsymbol{N} \cdot \boldsymbol{F}^{\mathrm{e\,tr}-1}\right). \tag{67}$$

To this point, no approximation has been introduced in the above stress-point integration algorithm whatsoever, so all the calculated slips and rotations are exact.

4. Multislip system

In a more general case the coarse-scale displacement increment $\Delta\widetilde{\boldsymbol{u}}$ may be large enough to trigger two or more slip systems. Some of these systems may be linearly dependent requiring the use of a more specialized filtering algorithm. We set aside the issue of redundant systems and assume for now that all active slip systems are linearly independent (we will address the issue of redundant systems later). If $\Delta\widetilde{\boldsymbol{u}}$ is large enough to trigger a secondary slip, then we need to: (a) identify the secondary slip system, and (b) accommodate a two-slip

(duplex) system. To simplify the equations, we shall assume for now that all slip directions define a forward motion. Later, we shall generalize the algorithm and accommodate backward slip by re-introducing the sign function, like we did in the previous section.

4.1. Identifying a secondary slip system

Assume that the coarse-scale displacement increment is applied as a ramp function according to $t\Delta\widetilde{\boldsymbol{u}}$, where t is a pseudo-time variable that varies from $[0,1]$. The coarse-scale deformation gradients then vary according to the equations

$$\boldsymbol{F}_t^{\mathrm{e\ tr}} = \boldsymbol{F}_n^{\mathrm{e\ tr}} + t\frac{\partial \Delta\widetilde{\boldsymbol{u}}}{\partial \boldsymbol{X}}, \quad \boldsymbol{f}_t^{\mathrm{e\ tr}} = \boldsymbol{1} + t\frac{\partial \Delta\widetilde{\boldsymbol{u}}}{\partial \widetilde{\boldsymbol{x}}_n}. \tag{68}$$

This means that the primary slip direction $\boldsymbol{m}^{(1)}$ varies according to the relation

$$\boldsymbol{m}_t^{(1)} = \boldsymbol{f}_t^{\mathrm{e\ tr}} \cdot \boldsymbol{m}_n^{(1)} / \|\boldsymbol{f}_t^{\mathrm{e\ tr}} \cdot \boldsymbol{m}_n^{(1)}\|, \tag{69}$$

whereas the unit normal $\boldsymbol{n}^{(1)}$ varies according to the equation

$$\boldsymbol{n}_t^{(1)} = \boldsymbol{n}_n^{(1)} \cdot \boldsymbol{f}_t^{\mathrm{e\ tr\text{-}1}} / \|\boldsymbol{n}_n^{(1)} \cdot \boldsymbol{f}_t^{\mathrm{e\ tr\text{-}1}}\|, \tag{70}$$

where superscript '(1)' pertains to the primary slip system, assumed herein to be active right at the beginning of the load increment. From the previous section, the elastic component of relative deformation gradient in the presence of single slip varies according to

$$\boldsymbol{f}_t^{\mathrm{e}} = \boldsymbol{f}_t^{\mathrm{e\ tr}} - \Delta\zeta_t^{(1)} \boldsymbol{m}^{(1)} \otimes \boldsymbol{N}^{(1)} \cdot \boldsymbol{F}_n^{\mathrm{e\ tr}-1}, \tag{71}$$

where

$$\Delta\zeta_t^{(1)} = \zeta_t^{(1)} - \zeta_n^{(1)} \|\boldsymbol{f}_t^{\mathrm{e\ tr}} \cdot \boldsymbol{m}_n^{(1)}\| \tag{72}$$

is the slip increment, which is seen to depend on the pseudo-time variable t as well. We can thus calculate the elastic left Cauchy-Green deformation tensor as

$$\boldsymbol{b}_t^{\mathrm{e}} = \boldsymbol{f}_t^{\mathrm{e}} \cdot \boldsymbol{b}_n^{\mathrm{e}} \cdot \boldsymbol{f}_t^{\mathrm{eT}}, \tag{73}$$

from which the Kirchhoff stress tensor $\boldsymbol{\tau}_t$ can be determined from the hyperelastic constitutive equation. The incremental slip $\Delta\zeta_t^{(1)}$ is obtained from the discrete consistency condition

$$\psi_t^{(1)} \boldsymbol{m}_t^{(1)} \otimes \boldsymbol{n}_t^{(1)} : \boldsymbol{\tau}_t - (\tau_{Yn} + \Delta\zeta_t^{(1)} \mathcal{H}_{\mathcal{D}}) = 0. \tag{74}$$

The above stress-integration algorithm is exact provided that t does not trigger a secondary slip.

Now, suppose we want to determine the value of t that is large enough to trigger a secondary slip system β. The search for the critical slip system entails testing all inactive systems for yielding and identifying the specific system that gives the minimum triggering value of t. For any potential secondary slip system β the slip direction varies according to the equation

$$\boldsymbol{m}_t^{(\beta)} = \boldsymbol{f}_t^{\mathrm{e\ tr}} \cdot \boldsymbol{m}_n^{(\beta)} / \|\boldsymbol{f}_t^{\mathrm{e\ tr}} \cdot \boldsymbol{m}_n^{(\beta)}\|, \tag{75}$$

whereas the unit normal varies according to the relation

$$\boldsymbol{n}_t^{(\beta)} = \boldsymbol{n}_n^{(\beta)} \cdot \boldsymbol{f}_t^{\mathrm{e\ tr}-1} / \|\boldsymbol{n}_n^{(\beta)} \cdot \boldsymbol{f}_t^{\mathrm{e\ tr}-1}\|. \tag{76}$$

We recall that the coarse-scale relative deformation gradient $\boldsymbol{f}^{\mathrm{e\ tr}}$ rotates all slip systems in the crystal lattice exactly as $\boldsymbol{f}^{\mathrm{e}}$ provided that yielding in the crystal is restricted to that of single slip. The critical t required for yielding of any system β then satisfies the yield condition

$$\psi_t^{(\beta)} \boldsymbol{m}_t^{(\beta)} \otimes \boldsymbol{n}_t^{(\beta)} : \boldsymbol{\tau}_t - (\tau_{Yn} + \Delta\zeta_t^{(1)} \mathcal{H}_{\mathcal{D}}) = 0. \tag{77}$$

Eqs. (74) and (77) must be solved simultaneously to determine the value of t that produces initial yielding on any potential secondary slip system. The true secondary slip system is one for which the triggering value of t is minimum.

We summarize the required iterative solution for determining the secondary slip system. Dropping subscript t for brevity and re-introducing the sign function, we calculate the elastic relative deformation gradient as (cf. (71))

$$\boldsymbol{f}^{\mathrm{e}} = \boldsymbol{f}^{\mathrm{e\ tr}} - \Delta\zeta^{(1)}\psi^{(1)}\boldsymbol{m}^{(1)} \otimes \boldsymbol{N}^{(1)} \cdot \boldsymbol{F}_n^{\mathrm{e\ tr}-1}. \tag{78}$$

Let

$$\boldsymbol{r}^{(\cdot)} = \mathrm{sym}(\boldsymbol{m}^{(\cdot)} \otimes \boldsymbol{n}^{(\cdot)}). \tag{79}$$

Then solve $\boldsymbol{R}(\boldsymbol{x}^*) = \boldsymbol{0}$ for the unknown $\boldsymbol{x}^*$, where

$$\boldsymbol{R} = \boldsymbol{R}(\boldsymbol{x}) = \left\{ \begin{matrix} R_1 \\ R_2 \end{matrix} \right\} = \left\{ \begin{matrix} \psi^{(1)}\boldsymbol{r}^{(1)} : \boldsymbol{\tau} - \tau_{Y_n} - x_1\mathcal{H}_{\mathcal{D}} \\ \psi^{(\beta)}\boldsymbol{r}^{(\beta)} : \boldsymbol{\tau} - \tau_{Y_n} - x_1\mathcal{H}_{\mathcal{D}} \end{matrix} \right\} \tag{80}$$

is the local residual vector, and

$$\boldsymbol{x} = \left\{ \begin{matrix} x_1 \\ x_2 \end{matrix} \right\} = \left\{ \begin{matrix} \Delta\zeta^{(1)} \\ t \end{matrix} \right\} \tag{81}$$

is the local vector of unknowns. The local tangent operator for Newton iteration is

$$\boldsymbol{R}'(\boldsymbol{x}) = \begin{bmatrix} R_{1,1} & R_{1,2} \\ R_{2,1} & R_{2,2} \end{bmatrix}. \tag{82}$$

The tensor $\boldsymbol{r}$ depends on $x_2 = t$ alone, and not on $x_1 = \Delta\zeta^{(1)}$, so we evaluate

$$R_{1,1} = \frac{1}{2}\psi^{(1)}\boldsymbol{r}^{(1)} : \boldsymbol{\varphi}^{\mathrm{e}} : \boldsymbol{b}^{\mathrm{e}}_{,1} - \mathcal{H}_{\mathcal{D}} \tag{83}$$

$$R_{2,1} = \frac{1}{2}\psi^{(\beta)}\boldsymbol{r}^{(\beta)} : \boldsymbol{\varphi}^{\mathrm{e}} : \boldsymbol{b}^{\mathrm{e}}_{,1} - \mathcal{H}_{\mathcal{D}}. \tag{84}$$

On the other hand, the hardening law depends on $x_1 = \Delta\zeta^{(1)}$ alone, and not on $x_2 = t$, so we determine

$$R_{1,2} = \psi^{(1)}\boldsymbol{r}^{(1)}_{,2} : \boldsymbol{\tau} + \frac{1}{2}\psi^{(1)}\boldsymbol{r}^{(1)} : \boldsymbol{\varphi}^{\mathrm{e}} : \boldsymbol{b}^{\mathrm{e}}_{,2} \tag{85}$$

$$R_{2,2} = \psi^{(\beta)}\boldsymbol{r}^{(\beta)}_{,2} : \boldsymbol{\tau} + \frac{1}{2}\psi^{(\beta)}\boldsymbol{r}^{(\beta)} : \phi^{\mathrm{e}} : \boldsymbol{b}^{\mathrm{e}}_{,2}. \tag{86}$$

To find the derivatives of $\boldsymbol{r}$, we note that

$$\boldsymbol{r}_{,2} = \boldsymbol{r}_{,t} = \mathrm{sym}(\boldsymbol{m} \otimes \boldsymbol{n}_{,t} + \boldsymbol{m}_{,t} \otimes \boldsymbol{n}), \tag{87}$$

where

$$\boldsymbol{m}_{,t} = \frac{\boldsymbol{f}^{\mathrm{e\ tr}}_{,t} \cdot \boldsymbol{m}_n}{\|\boldsymbol{f}^{\mathrm{e\ tr}} \cdot \boldsymbol{m}_n\|} \cdot (\boldsymbol{1} - \boldsymbol{m} \otimes \boldsymbol{m}) \tag{88}$$

and

$$\boldsymbol{n}_{,t} = \frac{\boldsymbol{n}_n \cdot \boldsymbol{f}^{\mathrm{e\ tr}-1}_{,t}}{\|\boldsymbol{n}_n \cdot \boldsymbol{f}^{\mathrm{e\ tr}-1}\|} \cdot (\boldsymbol{1} - \boldsymbol{n} \otimes \boldsymbol{n}). \tag{89}$$

So, the derivatives of the relative deformation gradients are

$$\boldsymbol{f}^{\mathrm{e\ tr}}_{,t} = \frac{\partial\Delta\widetilde{\boldsymbol{u}}}{\partial\widetilde{\boldsymbol{x}}_n}, \quad \boldsymbol{f}^{\mathrm{e\ tr}-1}_{,t} = -\boldsymbol{f}^{\mathrm{e\ tr}-1} \cdot \frac{\partial\Delta\widetilde{\boldsymbol{u}}}{\partial\widetilde{\boldsymbol{x}}_n} \cdot \boldsymbol{f}^{\mathrm{e\ tr}-1}. \tag{90}$$

The derivatives of $\boldsymbol{b}^{\mathrm{e}}$ follow from the chain rule

$$\boldsymbol{b}^{\mathrm{e}}_{,i} = \boldsymbol{f}^{\mathrm{e}}_{,i} \cdot \boldsymbol{b}^{\mathrm{e}}_n \cdot \boldsymbol{f}^{\mathrm{eT}} + \boldsymbol{f}^{\mathrm{e}} \cdot \boldsymbol{b}^{\mathrm{e}}_n \cdot \boldsymbol{f}^{\mathrm{eT}}_{,i}, \quad i = 1, 2. \tag{91}$$

We note that

$$\boldsymbol{f}^{\mathrm{e}} = \boldsymbol{1} + x_2 \frac{\partial \Delta \widetilde{\boldsymbol{u}}}{\partial \widetilde{\boldsymbol{x}}_n} - x_1 \psi^{(1)} \boldsymbol{m}^{(1)} \otimes \boldsymbol{N}^{(1)} \cdot \boldsymbol{F}_n^{\mathrm{e\ tr}-1}. \tag{92}$$

So,

$$\boldsymbol{f}^{\mathrm{e}}_{,1} = \boldsymbol{f}^{\mathrm{e}}_{,\Delta\zeta^{(1)}} = -\psi^{(1)} \boldsymbol{m}^{(1)} \otimes \boldsymbol{N}^{(1)} \cdot \boldsymbol{F}_n^{\mathrm{e\ tr}-1} \tag{93}$$

and

$$\boldsymbol{f}^{\mathrm{e}}_{,2} = \boldsymbol{f}^{\mathrm{e}}_{,t} = \frac{\partial \Delta \widetilde{\boldsymbol{u}}}{\partial \widetilde{\boldsymbol{x}}_n} - \Delta\zeta^{(1)} \psi^{(1)} \boldsymbol{m}^{(1)}_{,t} \otimes \boldsymbol{N}^{(1)} \cdot \boldsymbol{F}_n^{\mathrm{e\ tr}-1}. \tag{94}$$

4.2. Duplex system

Consider a duplex (two-slip) system subjected to a conforming displacement field $\widetilde{\boldsymbol{u}}$. We define the slip systems by superscripts a and b. The kinematics of deformation is given by

$$\boldsymbol{u} = \overline{\boldsymbol{u}} + [\![\boldsymbol{u}^a]\!] H^a_{\mathcal{D}} + [\![\boldsymbol{u}^b]\!] H^b_{\mathcal{D}}, \quad H^{\circ}{}_{\mathcal{D}}(\boldsymbol{X}) = \begin{cases} 1 & \text{if } \boldsymbol{X} \in \mathcal{D}^{\circ}{}_{+} \\ 0 & \text{if } \boldsymbol{X} \in \mathcal{D}^{\circ}{}_{-} \end{cases}, \tag{95}$$

where $\circ$ denotes either slip system a or b, and $\mathcal{D}^{\circ}_{\pm}$ represents regions in the crystal lattice on the opposite sides of the glide planes. The Heaviside functions represent the two discontinuities.

In terms of the continuous and conforming displacement fields, $\overline{\boldsymbol{u}}$ and $\widetilde{\boldsymbol{u}}$, respectively, we find the following expressions for the elastic component of deformation gradients,

$$\boldsymbol{F}^{\mathrm{e}} = \boldsymbol{F}^{\mathrm{e\ tr}} - \zeta^a \psi^a \boldsymbol{m}^a \otimes \boldsymbol{N}^a - \zeta^b \psi^b \boldsymbol{m}^b \otimes \boldsymbol{N}^b \tag{96}$$

at any time $t > t_n$, and

$$\boldsymbol{F}^{\mathrm{e}}_n = \boldsymbol{F}^{\mathrm{e\ tr}}_n - \zeta^a_n \psi^a_n \boldsymbol{m}^a_n \otimes \boldsymbol{N}^a - \zeta^b_n \psi^b_n \boldsymbol{m}^b_n \otimes \boldsymbol{N}^b \tag{97}$$

at time t_n. The sign functions are defined in the obvious way,

$$\psi^a = \mathrm{sign}((\boldsymbol{m}^a \otimes \boldsymbol{n}^a) : \boldsymbol{\tau}), \quad \psi^b = \mathrm{sign}((\boldsymbol{m}^b \otimes \boldsymbol{n}^b) : \boldsymbol{\tau}) \tag{98}$$

and so on. Note that $\boldsymbol{F}^{\mathrm{e}}_n$ is known and can be readily inverted to give

$$\boldsymbol{f}^{\mathrm{e}} = \boldsymbol{F}^{\mathrm{e\ tr}} \cdot \boldsymbol{F}_n^{\mathrm{e}-1} - \zeta^a \psi^a \boldsymbol{m}^a \otimes \boldsymbol{N}^a \cdot \boldsymbol{F}_n^{\mathrm{e}-1} - \zeta^b \psi^b \boldsymbol{m}^b \otimes \boldsymbol{N}^b \cdot \boldsymbol{F}_n^{\mathrm{e}-1}. \tag{99}$$

Due to the presence of the secondary slip, the rotation induced by $\boldsymbol{f}^{\mathrm{e\ tr}}$ is no longer the same as the rotation induced by $\boldsymbol{f}^{\mathrm{e}}$.

Noting that

$$\boldsymbol{m}^a = \boldsymbol{f}^{\mathrm{e}} \cdot \boldsymbol{m}^a_n / \|\boldsymbol{f}^{\mathrm{e}} \cdot \boldsymbol{m}^a_n\|, \quad \boldsymbol{m}^b = \boldsymbol{f}^{\mathrm{e}} \cdot \boldsymbol{m}^b_n / \|\boldsymbol{f}^{\mathrm{e}} \cdot \boldsymbol{m}^b_n\|, \tag{100}$$

we view Eq. (99) as a system of nine scalar equations in eleven scalar unknowns, namely, the nine elements of $\boldsymbol{f}^{\mathrm{e}}$ and the two slips ζ^a and ζ^b. The consistency conditions provide the two remaining equations, which we write in residual form, using Taylor hardening [60], as

$$R_{\circ} = (\psi^{\circ} \boldsymbol{m}^{\circ} \otimes \boldsymbol{n}^{\circ}) : \boldsymbol{\tau} - \left(\tau_{Yn} + \sum_{\circ = a,b} \Delta\zeta^{\circ} \mathcal{H} \right) \to 0, \quad \circ = a, b, \tag{101}$$

where

$$\Delta\zeta^{\circ} = \zeta^{\circ} - \zeta^{\circ}_n \|\boldsymbol{f}^{\mathrm{e}} \cdot \boldsymbol{m}^{\circ}_n\|, \quad \circ = a, b \tag{102}$$

and $\mathcal{H}$ is the plastic modulus. As before, the Kirchhoff stress tensor $\boldsymbol{\tau}$ can be obtained from the sequence of calculations $\boldsymbol{f}^{\mathrm{e}} \to \boldsymbol{b}^{\mathrm{e}} \to \boldsymbol{\tau}$. Since no approximation has been introduced in the above derivations, we expect the calculated slips and crystal rotations to be exact.

A straightforward solution would be to consider a system of eleven nonlinear equations in eleven unknowns. However, the expected computational effort would be significant, and so in what follows we propose an alternative iterative solution strategy. The proposed technique consists of two levels of iteration: an outer loop that updates the estimate of $\boldsymbol{f}^{\mathrm{e}}$, and an inner loop that solves the two slips by Newton iteration. Box 1 shows a flow chart of the proposed iterative algorithm. The algorithm is driven by $\boldsymbol{F}^{\mathrm{e\ tr}}$, and final convergence of the iteration is checked in Step 6. The residuals calculated in Step 6 pertain to the convergence properties of the outer loop, which employs the method of successive substitution for updating the value of $\boldsymbol{f}^{\mathrm{e}}$. The inner loop would have its own convergence profile in Step 7 reflecting the properties of Newton's method. From the known properties of the two iterative algorithms, we expect the rate of convergence of the inner loop to be faster than that of the outer loop.

Box 1. Exact Algorithm: nested iterations employing the method of successive substitution for $\boldsymbol{f}^{\mathrm{e}}$ (outer loop) combined with Newton iteration for ζ^a and ζ^b (inner loop), with slip vectors $\boldsymbol{m}^\circ$ calculated from the rotation of the crystal lattice.

Step 1. Initialize $\boldsymbol{F}^{\mathrm{e\ tr}} = \boldsymbol{F}_n^{\mathrm{e\ tr}} + \partial \Delta\widetilde{\boldsymbol{u}}/\partial \boldsymbol{X}, \quad \boldsymbol{f}^{\mathrm{e}} = \boldsymbol{1}, \quad \zeta^a = \zeta_n^a, \quad \zeta^b = \zeta_n^b.$
Step 2. Rotate $\boldsymbol{m}^\circ = \boldsymbol{f}^{\mathrm{e}} \cdot \boldsymbol{m}_n^\circ / \|\boldsymbol{f}^{\mathrm{e}} \cdot \boldsymbol{m}_n^\circ\|$ for $\circ = a, b$.
Step 3. Solve $\boldsymbol{F}^{\mathrm{e}} = \boldsymbol{F}^{\mathrm{e\ tr}} - \sum_{\circ=a,b} \zeta^\circ \psi^\circ \boldsymbol{m}^\circ \otimes \boldsymbol{N}^\circ$
$\boldsymbol{f}^{\mathrm{e}} = \boldsymbol{F}^{\mathrm{e}} \cdot \boldsymbol{F}_n^{\mathrm{e}-1}$.
Step 4. Compute $\boldsymbol{f}^{\mathrm{e}} \to \boldsymbol{b}^{\mathrm{e}} \to \boldsymbol{\tau}$.
Step 5. Compute residuals R_a and R_b.
Step 6. Check for convergence: if $\mathcal{R} = \sqrt{R_a^2 + R_b^2} < \mathrm{TOL}$, exit.
Step 7. Else, iterate $R_a \to 0$ and $R_b \to 0$ for ζ^a and ζ^b.
Step 8. Go to Step 2.

The co-rotational slips ζ^a and ζ^b can be solved by imposing the consistency conditions on the two slip systems. Assuming a Taylor hardening law [60], we obtain the pair of equations

$$R_\circ = \psi^\circ [(\boldsymbol{m}^\circ \otimes \boldsymbol{n}^\circ) : \boldsymbol{\tau}] - \left(\tau_{Yn} + \sum_{\circ=a,b} \Delta\zeta^\circ \mathcal{H} \right) \to 0, \quad \circ = a, b, \tag{103}$$

where $\Delta\zeta^\circ$ are the incremental slips given in (101) and $\mathcal{H}$ is the plastic modulus. Note that the Newton iteration takes place for a fixed $\boldsymbol{f}^{\mathrm{e}}$, which means the resulting 2×2 tangent operator is fairly straightforward to solve. In abbreviated form, we have

$$R_{\circ,\bullet} = \psi^\circ \left[(\boldsymbol{m}^\circ \otimes \boldsymbol{n}^\circ) : \frac{\partial \boldsymbol{\tau}}{\partial \zeta^\bullet} \right] - \mathcal{H}, \quad \circ, \bullet = a, b. \tag{104}$$

The derivative of $\boldsymbol{\tau}$ is

$$\frac{\partial \boldsymbol{\tau}}{\partial \zeta^\bullet} = \boldsymbol{\alpha}^{\mathrm{e}} : \left(\frac{\partial \boldsymbol{f}^{\mathrm{e}}}{\partial \zeta^\bullet} \cdot \boldsymbol{f}^{\mathrm{e}-1} \right), \quad \bullet = a, b, \tag{105}$$

where

$$\frac{\partial \boldsymbol{f}^{\mathrm{e}}}{\partial \zeta^\bullet} = -\psi^\bullet \boldsymbol{m}^\bullet \otimes \boldsymbol{N}^\bullet \cdot \boldsymbol{F}_n^{\mathrm{e}-1}, \quad \bullet = a, b \tag{106}$$

and $\boldsymbol{f}^{\mathrm{e}}$ can be inverted directly. As shown in the numerical examples presented later in this paper, the structure of the composite techniques produces a stable iterative solution.

4.2.1. Alternative Algorithm #1

Although an exact solution can be obtained for the problem at hand, it comes with a price in the form of increased computational cost. In what follows, we explore a simpler alternative algorithm consisting of one Newton iteration loop for the slips, and no outer iteration loop. The idea is illustrated in Box 2 and can be summarized succinctly as follows: the slip vectors are determined from the overall rotation of the crystal rather than from the rotation of the crystal lattice. Therefore, there is no need to iterate for the rotation of the slip vectors. In a way, this idea is similar to that employed in classical return mapping algorithm of computational plasticity, where the direction of the final stress tensor is determined from the direction of the elastic stress predictor.

4.2.2. Alternative Algorithm #2

As an additional alternative algorithm, we construct an even simpler iterative scheme that has the form of that developed for single-slip systems, i.e., the linearized version (78). We note that for single-slip systems, this linearized form is exact; however, for multislip systems it is no longer exact as illustrated in the developments below.

Box 2. Alternative Algorithm #1: one-level Newton iteration for slips ζ^a and ζ^b with slip vectors $\boldsymbol{m}^\circ$ calculated from the overall rotation of the crystal.

Step 1. Initialize $\boldsymbol{F}^{\mathrm{e\,tr}} = \boldsymbol{F}_n^{\mathrm{e\,tr}} + \partial\Delta\widetilde{\boldsymbol{u}}/\partial\boldsymbol{X}$, $\zeta^a = \zeta_n^a$, $\zeta^b = \zeta_n^b$.
Step 2. Rotate $\boldsymbol{m}^\circ = \boldsymbol{F}^{\mathrm{e\,tr}} \cdot \boldsymbol{M}^\circ / \|\boldsymbol{F}^{\mathrm{e\,tr}} \cdot \boldsymbol{M}^\circ\|$ for $\circ = a, b$.
Step 3. Solve $\boldsymbol{F}^{\mathrm{e}} = \boldsymbol{F}^{\mathrm{e\,tr}} - \sum_{\circ=a,b} \zeta^\circ \psi^\circ \boldsymbol{m}^\circ \otimes \boldsymbol{N}^\circ$
$\boldsymbol{f}^{\mathrm{e}} = \boldsymbol{F}^{\mathrm{e}} \cdot \boldsymbol{F}_n^{\mathrm{e}-1}$.
Step 4. Compute $\boldsymbol{f}^{\mathrm{e}} \to \boldsymbol{b}^{\mathrm{e}} \to \boldsymbol{\tau}$.
Step 5. Iterate $R_a \to 0$ and $R_b \to 0$ for ζ^a and ζ^b, and exit.

We assume that $\boldsymbol{f}^{\mathrm{e\,tr}}$ is an acceptable surrogate for $\boldsymbol{f}^{\mathrm{e}}$ in rotating the slip vectors. Hence, given the slips ζ^a and ζ^b, $\boldsymbol{f}^{\mathrm{e}}$ can be calculated explicitly from (99). We can determine the inverse of $\boldsymbol{F}_n^{\mathrm{e}}$ analytically, or, alternatively, by a recursive use of the Sherman–Morrison formula. Let

$$\boldsymbol{F}_{na}^{\mathrm{e}} = \boldsymbol{F}_n^{\mathrm{e\,tr}} - \zeta_n^a \psi_n^a \boldsymbol{m}_n^a \otimes \boldsymbol{N}^a; \tag{107}$$

then

$$\boldsymbol{F}_n^{\mathrm{e}} = \boldsymbol{F}_{na}^{\mathrm{e\,tr}} - \zeta_n^b \psi_n^b \boldsymbol{m}_n^b \otimes \boldsymbol{N}^b. \tag{108}$$

The respective inverses are

$$\boldsymbol{F}_{na}^{\mathrm{e}-1} = \boldsymbol{F}_n^{\mathrm{e\,tr}-1} + \zeta_n^a \boldsymbol{F}_n^{\mathrm{e\,tr}-1} \cdot \psi_n^a \boldsymbol{m}_n^a \otimes \boldsymbol{N}^a \cdot \boldsymbol{F}_n^{\mathrm{e\,tr}-1} \tag{109}$$

and

$$\boldsymbol{F}_n^{\mathrm{e}-1} = \boldsymbol{F}_{na}^{\mathrm{e\,tr}-1} + \zeta_n^b \boldsymbol{F}_{na}^{\mathrm{e\,tr}-1} \cdot \psi_n^b \boldsymbol{m}_n^b \otimes \boldsymbol{N}^b \cdot \boldsymbol{F}_{na}^{\mathrm{e\,tr}-1}. \tag{110}$$

Expanding the expressions above gives a polynomial expression for $\boldsymbol{f}^{\mathrm{e}}$ in ζ^a, ζ^b, ζ_n^a, and ζ_n^b. Now, if we ignore the higher-order terms of the polynomial and take only the linear terms, we get

$$\boldsymbol{f}^{\mathrm{e}} = \boldsymbol{f}^{\mathrm{e\,tr}} - \Delta\zeta^a \psi^a \boldsymbol{m}^a \otimes \boldsymbol{N}^a \cdot \boldsymbol{F}_n^{\mathrm{e\,tr}-1} - \Delta\zeta^b \psi^b \boldsymbol{m}^b \otimes \boldsymbol{N}^b \cdot \boldsymbol{F}_n^{\mathrm{e\,tr}-1}, \tag{111}$$

where

$$\Delta\zeta^a = \zeta^a - \zeta_n^a \|\boldsymbol{f}^{\mathrm{e\,tr}} \cdot \boldsymbol{m}_n^a\|, \quad \Delta\zeta^b = \zeta^b - \zeta_n^b \|\boldsymbol{f}^{\mathrm{e\,tr}} \cdot \boldsymbol{m}_n^b\| \tag{112}$$

and $\boldsymbol{f}^{\mathrm{e\,tr}} = \boldsymbol{F}^{\mathrm{e\,tr}} \cdot \boldsymbol{F}_n^{\mathrm{e\,tr}-1}$. Eq. (111) shows the classical predictor–corrector algorithm for $\boldsymbol{f}^{\mathrm{e}}$ with a form that is very much similar to that used for single-slip systems, namely, Eq. (78). This facilitates a convenient

implementation of the algorithm. As shown in Box 3, this linearized version of the algorithm can be used for single-slip and multislip systems simply by changing the index of summation.

Box 3. Alternative Algorithm #2: the linearized version. One-level Newton iteration for incremental slips $\Delta\zeta^a$ and $\Delta\zeta^b$ with slip vectors $\boldsymbol{m}^\circ$ calculated from the overall rotation of the crystal.

Step 1. Initialize $\boldsymbol{f}^{\mathrm{e\,tr}} = \boldsymbol{1} + \partial\Delta\widetilde{\boldsymbol{u}}/\partial\widetilde{\boldsymbol{x}}_n, \zeta^a = \zeta^a_n, \zeta^b = \zeta^b_n$.
Step 2. Rotate $\boldsymbol{m}^\circ = \boldsymbol{f}^{\mathrm{e\,tr}} \cdot \boldsymbol{m}^\circ_n / \|\boldsymbol{f}^{\mathrm{e\,tr}} \cdot \boldsymbol{m}^\circ_n\|$ for $\circ = a, b$.
Step 3. Solve $\boldsymbol{f}^{\mathrm{e}} = \boldsymbol{f}^{\mathrm{e\,tr}} - \sum_{\circ=a,b} \Delta\zeta^\circ \psi^\circ \boldsymbol{m}^\circ \otimes \boldsymbol{N}^\circ \cdot \boldsymbol{F}^{\mathrm{e\,tr}-1}_n$.
Step 4. Compute $\boldsymbol{f}^{\mathrm{e}} \to \boldsymbol{b}^{\mathrm{e}} \to \boldsymbol{\tau}$.
Step 5. Iterate $R_a \to 0$ and $R_b \to 0$ for $\Delta\zeta^a$ and $\Delta\zeta^b$, and exit.

4.3. General framework for multislip systems

Extending the two-slip framework to multislip systems is fairly straightforward. Let $N =$ number of linearly independent active slip systems. The elastic component of deformation gradient is

$$\boldsymbol{F}^{\mathrm{e}} = \boldsymbol{F}^{\mathrm{e\,tr}} - \sum_{\alpha=1}^{N} \zeta^\alpha \psi^\alpha \boldsymbol{m}^\alpha \otimes \boldsymbol{N}^\alpha \tag{113}$$

at any time $t > t_n$, and

$$\boldsymbol{F}^{\mathrm{e}}_n = \boldsymbol{F}^{\mathrm{e\,tr}}_n - \sum_{\alpha=1}^{N} \zeta^\alpha_n \psi^\alpha_n \boldsymbol{m}^\alpha_n \otimes \boldsymbol{N}^\alpha \tag{114}$$

at time t_n. Inverting $\boldsymbol{F}^{\mathrm{e}}_n$ gives

$$\boldsymbol{f}^{\mathrm{e}} = \boldsymbol{F}^{\mathrm{e}} \cdot \boldsymbol{F}^{\mathrm{e}-1}_n = \boldsymbol{F}^{\mathrm{e\,tr}} \cdot \boldsymbol{F}^{\mathrm{e}-1}_n - \sum_{\alpha=1}^{N} \zeta^\alpha \psi^\alpha \boldsymbol{m}^\alpha \otimes \boldsymbol{N}^\alpha \cdot \boldsymbol{F}^{\mathrm{e}-1}_n. \tag{115}$$

The co-rotational slips can be solved by imposing the consistency conditions on all the linearly independent active slip systems,

$$R_\alpha = \psi^\alpha [(\boldsymbol{m}^\alpha \otimes \boldsymbol{n}^\alpha) : \boldsymbol{\tau}] - \left(\tau_{Yn} + \sum_{\eta=1}^{N} \Delta\zeta^\eta \mathcal{H} \right) \to 0 \tag{116}$$

for $\alpha = 1, \ldots, N$, where $\Delta\zeta^\eta = \zeta^\eta - \zeta^\eta_n \|\boldsymbol{f}^{\mathrm{e\,tr}} \cdot \boldsymbol{m}^\eta_n\|$ as before.

To select the next linearly independent active system from a set of N active ones, we introduce once again the pseudo time variable t. The consistency conditions for all the active systems are

$$\psi^\alpha_t \boldsymbol{m}^\alpha_t \otimes \boldsymbol{n}^\alpha_t : \boldsymbol{\tau}_t - \left(\tau_{Yn} + \sum_{\eta=1}^{N} \Delta\zeta^\eta_t \mathcal{H} \right) = 0. \tag{117}$$

Combining these with the consistency condition for the next potentially active slip system β,

$$\psi^\beta_t \boldsymbol{m}^\beta_t \otimes \boldsymbol{n}^\beta_t : \boldsymbol{\tau}_t - \left(\tau_{Yn} + \sum_{\eta=1}^{N} \Delta\zeta^\eta_t \mathcal{H} \right) = 0, \tag{118}$$

we obtain a system of $(N+1)$ simultaneous nonlinear equations in N slip increments and the pseudo time variable t that can be solved iteratively by Newton iteration. For the exact solution, this Newton iteration forms

an inner loop, with the method of successive substitution loop nesting over it. For the two approximate solutions presented above, this Newton iteration is the only local loop in the stress-point integration algorithm. The outcome of the solution is the next slip system for which the triggering value of t is minimum.

The above developments fit nicely within the framework of the 'ultimate algorithm' developed previously for crystal plasticity in the infinitesimal deformation range [16]. This algorithm tracks the sequence of slip system activation, and is unconditionally convergent. For the infinitesimal formulation, the main format of the algorithm is as follows: the overall crystal stresses and plastic variables at time t_n are given, along with the overall incremental strain; the algorithm then returns the overall crystal stresses and plastic variables at time t_{n+1}. If the overall incremental strain is imposed as a ramp function, then the algorithm gives exact overall crystal stresses and plastic variables at t_{n+1}. All of the above features of the algorithm carry over to the finite deformation range. A summary of the algorithm is shown in Box 4. For reference, the reader may want to compare this box to Table 1 of Ref. [16].

Steps 1 and 2 of Box 1 are simple checks for plastic yielding or elastic unloading. Step 3 identifies the potentially active systems either at time t_n or at some other time $t \in (t_n, t_{n+1})$ after contact with the last yield surface has been detected. The calculations in Step 4 aim to identify the next active yield surface within the current time increment. There is no guarantee that the active constraints will remain active within a given load step, so Step 5 filters out the previously active systems that de-activate during the present load step. In Step 6, the condition $t_{\min}^{(\alpha)} > 1$ for all α implies that the present deformation increment is too small to activate new slip systems. Compared to the ultimate algorithm in the infinitesimal deformation range [16], we remark that the present algorithm does not employ the overall crystal elasto-plastic moduli tensor in the calculations. We also note that the plastic slips and $t^{(\alpha)}$ are always determined simultaneously in the finite deformation case (whereas they were determined sequentially in the infinitesimal deformation case).

Box 4. Ultimate algorithm for crystal plasticity in the finite deformation range.

Step 1. Compute $\boldsymbol{b}^{\mathrm{e\,tr}} = \boldsymbol{f}^{\mathrm{e\,tr}} \cdot \boldsymbol{b}_n^{\mathrm{e}} \cdot \boldsymbol{f}^{\mathrm{e\,tr}}$ and $\boldsymbol{\tau}^{\mathrm{tr}} = \boldsymbol{\tau}(\boldsymbol{b}^{\mathrm{e\,tr}})$, and assemble $\mathcal{J}^{\mathrm{tr}} = \{\beta \mid \psi^{(\beta)}(\boldsymbol{m}^{(\beta)} \otimes \boldsymbol{n}^{(\beta)}) : \boldsymbol{\tau}^{\mathrm{tr}} - \tau_{Yn} > 0\}$.

Step 2. Check: $\mathcal{J}^{\mathrm{tr}} = \varnothing$? Yes, elastic response: set $\boldsymbol{b}^{\mathrm{e}} = \boldsymbol{b}^{\mathrm{e\,tr}}$, $\tau_Y = \tau_{Yn}$, and exit.

Step 3. Set $\mathcal{J}_{\mathrm{act}} = \{\beta \mid \psi^{(\beta)}(\boldsymbol{m}_n^{(\beta)} \otimes \boldsymbol{n}_n^{(\beta)}) : \boldsymbol{\tau}_n - \tau_{Yn} = 0\}$ and select $\overline{\mathcal{J}}_{\mathrm{act}} \subset \mathcal{J}_{\mathrm{act}}$.

Step 4. Solve iteratively for $\Delta\zeta^{(\beta)}$ and $t^{(\alpha)}$ for all $\beta \in \overline{\mathcal{J}}_{\mathrm{act}}$ and for all $\alpha \in \mathcal{J} \setminus \overline{\mathcal{J}}_{\mathrm{act}}$.

Step 5. If $\Delta\zeta^{(\beta)} < 0$, drop $\Delta\zeta_{\min}^{(\beta)}$ from $\overline{\mathcal{J}}_{\mathrm{act}}$ and go to Step 4.

Step 6. Check: is $t_{\min}^{(\alpha)} > 1$? Yes, set $t = 1$, solve for $\Delta\zeta^{(\beta)}, \boldsymbol{b}^{\mathrm{e}}$, and τ_Y, and exit.

Step 7. No, set $t = t_{\min}^{(\beta)}, \Delta\zeta_n^{(\beta)} \leftarrow \Delta\zeta^{(\beta)}, \boldsymbol{b}_n^{\mathrm{e}} \leftarrow \boldsymbol{b}^{\mathrm{e}}$, and $\tau_{Yn} \leftarrow \tau_Y$.

Step 8. Set $\Delta\widetilde{\boldsymbol{u}} \leftarrow (1-t)\Delta\widetilde{\boldsymbol{u}}$ and go to Step 3.

5. Numerical examples

For purposes of analysis, we consider the general form of an f.c.c. crystal rotated by Euler angles to create three different crystal orientations. Euler angles are shown in Fig. 4 and consist of a rotation of θ about the Y-axis followed by a rotation of ϕ about the Z_c axis. The slip systems considered are summarized in Table 1, and the crystal orientations are shown in Table 2. As an illustration, slip system #1 has the general form of an f.c.c. slip direction $\{110\}$ and slip normal $\{111\}$. To understand the crystal responses and assess the performance of the algorithms in single and double slips, some slip systems in the crystal have been suppressed. However, a numerical example is also included in which all available slip systems of an f.c.c. crystal are allowed to activate.

Table 1
Vectors $\boldsymbol{M}$ and $\boldsymbol{N}$, where $a = 1/\sqrt{2}, b = 1/\sqrt{3}$.

System	$\boldsymbol{M}$	$\boldsymbol{N}$
1	$\{a, -a, 0\}$	$\{b, b, b\}$
2	$\{a, 0, -a\}$	$\{b, -b, b\}$
3	$\{0, a, a\}$	$\{-b, b, -b\}$
4	$\{0, a, -a\}$	$\{b, b, b\}$

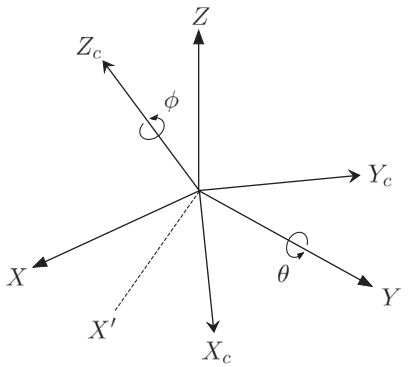

Fig. 4. Euler angles defining crystal axes (X_c, Y_c, Z_c) relative to the fixed system (X, Y, Z) in the reference configuration.

Table 2
Euler angles in degrees for three different crystal orientations.

Orientation	θ	ϕ
1	15	0
2	30	15
3	30	30

5.1. Single-slip deformation

As a first example, we consider the following conforming displacement field applied to a crystal

$$\widetilde{u}_1 = kX_1, \quad \widetilde{u}_2 = -0.5kX_2, \quad \widetilde{u}_3 = -0.5kX_3,$$

where k is a pseudo-time variable that increases with deformation. The above displacement field subjects the crystal to uniaxial tension. We consider deformation in single slip by suppressing all slip systems except for slip system #1. For the crystal lattice, we assume Young's modulus $E = 1500$ MPa and Poisson's ratio $\nu = 1/3$ (typical of shale, a sedimentary rock with significant crystalline inclusions). For plastic slip, we take a yield strength $\tau_Y = 10$ MPa and no hardening (i.e., perfect plasticity).

Fig. 5 shows the variation of the second Piola–Kirchhoff stress component 11 versus the Green–Lagrange strain component 11 for the three different crystal orientations, with only slip system #1 allowed to activate. It is evident that the orientation of a slip system does exert a strong influence on the resistance of the crystal to deformation. Crystal orientations #1 and #2 show pronounced geometric softening. We note that this type of softening is unique to the finite deformation solution and is not observed in infinitesimal solutions. Identical stress–strain curves were obtained irrespective of the loading step size, affirming the fact that the numerical algorithm for single-slip crystal plasticity is exact.

Fig. 6 shows the variation of slip with imposed strain for different crystal orientations. The more favorable the crystal orientation to imposed deformation, the greater is the magnitude of slip. For the record, the slip presented in the figure is the co-rotational slip ζ, which is measured in the current configuration, whereas the

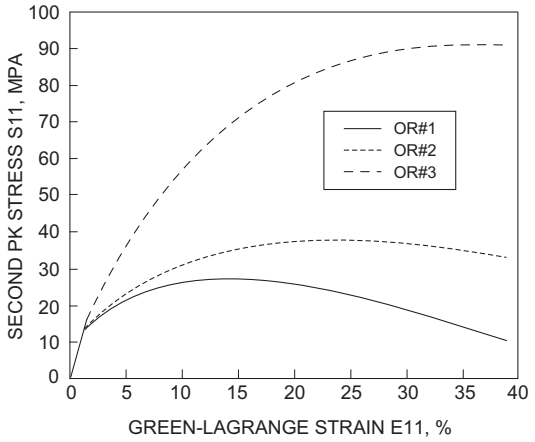

Fig. 5. Exact variation of second Piola–Kirchhoff stress versus Green–Lagrange strain for single-slip crystals under uniaxial tension.

horizontal axis is the Almansi strain. The Lagrangian slip γ in the reference configuration can be obtained from the slip ζ by applying a pull-back of the stretching of the crystal lattice.

Table 3 shows the convergence profiles of the local Newton iteration used to determine the plastic slips. These profiles are typical and do not change with the load size. The algorithm required a maximum of three iterations even for larger step sizes, indicating an efficient iterative solution.

5.2. Duplex system

This problem is the same as in the previous example except that we now release slip system #2 along with slip system #1. For all three crystal orientations, the sequence of slip activation is system #1 triggered first, followed by system #2. The imposed deformation and crystal properties are the same as in the previous example.

Fig. 7 shows the variation of the second Piola–Kirchhoff stress component 11 with Green–Lagrange strain component 11 derived from the exact solution. The figure indicates that geometric softening is more pronounced in a duplex system compared to the corresponding single-slip system. In fact, crystal Orientation #1 has experienced complete geometric softening at a strain value of approximately 15%. In addition, the orientation of the crystal generally impacts the timing of yielding of both the primary and secondary slip systems. On the other hand, Fig. 12 shows that the primary co-rotational slips are reduced by the development

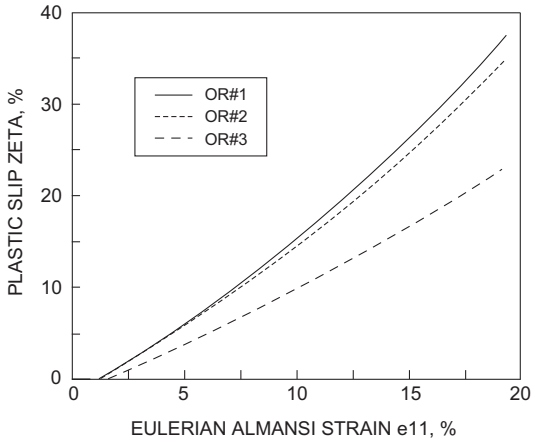

Fig. 6. Exact variation of plastic slip ζ versus Eulerian Almansi strain for single-slip crystals under uniaxial tension.

Table 3
Convergence profile of Newton iteration for single-slip crystal plasticity in uniaxial tension. Displayed errors are relative norms of residual vector normalized with respect to initial values.

Vertical strain (%)	Iteration	Orientation 1	Orientation 2	Orientation 3
5	1	1.00e+00	1.00e+00	1.00e+00
	2	1.33e−05	1.27e−05	8.98e−06
	3	1.47e−13	1.77e−13	6.79e−15
10	1	1.00e+00	1.00e+00	1.00e+00
	2	1.29e−05	1.22e−05	8.37e−06
	3	8.27e−14	1.96e−13	2.25e−13
15	1	1.00e+00	1.00e+00	1.00e+00
	2	1.26e−05	1.17e−05	7.84e−06
	3	3.75e−13	1.18e−13	1.11e−13
20	1	1.00e+00	1.00e+00	1.00e+00
	2	1.23e−05	1.12e−05	7.37e−06
	3	5.43e−14	4.01e−14	7.09e−14
25	1	1.00e+00	1.00e+00	1.00e+00
	2	1.20e−05	1.08e−05	6.96e−06
	3	2.98e−13	1.65e−13	1.57e−14
30	1	1.00e+00	1.00e+00	1.00e+00
	2	1.17e−05	1.03e−05	6.59e−06
	3	2.41e−14	8.20e−14	2.78e−13
40	1	1.00e+00	1.00e+00	1.00e+00
	2	1.11e−05	9.59e−06	5.95e−06
	3	3.12e−13	1.62e−13	3.17e−13

of secondary slips. In this case, plastic deformations are shared by the primary and secondary slips, resulting in softer stress–strain responses even though the developed primary co-rotational slips are smaller.

We note that to obtain the exact solution, the algorithm must first determine the contact yield point leading to the duplex system, and then the slip directions must be rotated by the elastic component of deformation gradient iteratively using the nested iteration loops shown in Box 1. Therefore, compared to the two alternative algorithms presented in the previous section, the exact solution requires greater computational effort. To get a feel for the convergence rate of the method of successive substitution, which is used to iterate for $\boldsymbol{f}^{\mathrm{e}}$, we summarize in Table 4 the dissipation of the scalar residual function $\mathcal{R}$ in Step 6 of Box 1. Convergence is still fast, but not quadratic. In general, the iterations are stable and convergent in all cases, indicating that the nonlinear relation between the slip vector $\boldsymbol{m}$ and the elastic relative deformation gradient $\boldsymbol{f}^{\mathrm{e}}$ is not too strong. The

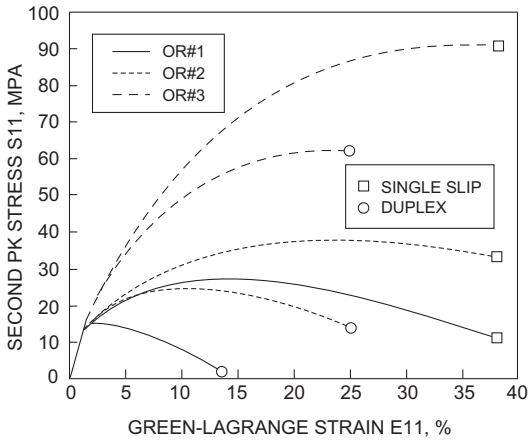

Fig. 7. Exact variation of second Piola–Kirchhoff stress versus Green–Lagrange strain for two-slip crystals under uniaxial tension. For comparison, single-slip responses are also shown.

convergence of Newton iteration in Step 7 of Box 1 remains rapid and is similar to the profile shown Table 3, i.e., the solutions converged to machine precision in 3 iterations. No sensitivity to load steps has been observed in all cases, a hallmark of an exact solution.

We now demonstrate the accuracy of the two alternative algorithms presented in the previous section. We recall that: (a) Algorithm #1 simply substitutes the rotation of the crystal in lieu of the rotation of the crystal lattice for purposes of updating the orientation of the plastic slip vector $\boldsymbol{m}$; and (b) Algorithm #2 is the linearized version of Algorithm #1 in which the higher-order terms of the polynomial expression for the co-rotational plastic slips are ignored. In single slips, the two algorithms coincide and lead to the same exact solution; in multiple slips, they are not the same and only represent approximate solutions. However, in the examples below we show that the two approximate solutions are indeed highly accurate. (See Fig. 8).

Fig. 9 compares the exact solutions with the approximate solutions calculated with Algorithm #1 for three different crystal orientations in double-slip yield mode. For purposes of plotting this figure, the incremental Green–Lagrange strain component 11 was set equal to 0.1%. However, it must be noted that the stress–strain responses do not depend on the load increment since the contact yield stresses are calculated exactly, and since the analytical expressions for the exact and approximate algorithms are integrated also exactly. In other words, even if we refined or coarsened the load increment we would obtain the same stress–strain response. We see from the figure that the difference between the exact and approximate solutions are very small even for large values of strain.

Table 4
Convergence profile of the method of successive substitution for double-slip crystal plasticity in uniaxial tension. Note that Orientation #1 experienced complete geometric softening beyond a vertical strain of 15%. Displayed errors are relative norms of residual vector, $\mathcal{R}$, normalized with respect to initial values, $\mathcal{R}_0$.

Vertical strain (%)	Iteration	Orientation 1	Orientation 2	Orientation 3
5	1	1.00e+00	1.00e+00	1.00e+00
	2	1.52e−02	3.73e−02	4.82e−02
	3	3.22e−04	3.57e−04	6.01e−04
	4	1.88e−06	6.84e−06	7.40e−06
	5	3.99e−08	1.29e−07	1.19e−07
	6	4.61e−10	9.24e−10	1.10e−09
	7	–	–	2.36e−11
10	1	1.00e+00	1.00e+00	1.00e+00
	2	2.19e−02	6.10e−02	8.96e−02
	3	1.16e−03	1.36e−03	2.62e−03
	4	1.40e−05	6.77e−05	7.63e−05
	5	3.71e−07	2.60e−06	2.88e−06
	6	5.59e−09	4.12e−09	6.05e−08
	7	2.71e−10	5.83e−11	3.25e−09
	8	–	–	5.32e−11
15	1	1.00e+00	1.00e+00	1.00e+00
	2	2.86e−02	8.83e−02	1.30e−01
	3	2.31e−03	3.15e−03	5.89e−03
	4	5.27e−05	2.02e−04	2.39e−04
	5	1.09e−06	1.24e−05	1.40e−05
	6	2.46e−08	3.05e−07	4.16e−07
	7	4.57e−10	4.08e−08	3.43e−08
	8	–	1.04e−09	8.76e−10
	9	–	9.68e−11	–
20	1	–	1.00e+00	1.00e+00
	2	–	1.15e−01	1.68e−01
	⋮	⋮	⋮	⋮
	9	–	5.54e−10	5.09e−10
25	1	–	1.00e+00	1.00e+00
	2	–	1.15e−01	1.68e−01
	⋮	⋮	⋮	⋮
	10	–	2.22e−10	1.28e−10

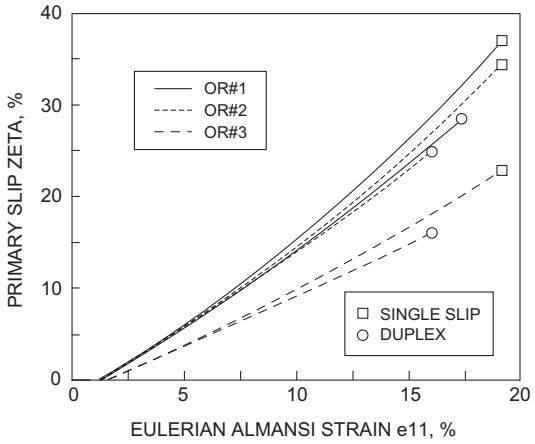

Fig. 8. Exact variation of co-rotational primary slip ζ versus Eulerian Almansi strain for two-slip crystals under uniaxial tension. For comparison, single-slip responses are also shown.

A more striking result is depicted in Fig. 10, where the solutions obtained from the two alternative algorithms are compared. Apart from the fact that the difference between the two approximate solutions is also very small, we see that Algorithm #2 appears to 'correct' the error produced by Algorithm #1, leading to a more accurate stress–strain response. In fact, the stress–strain curve generated with Algorithm #2 falls almost right on top of the curve generated with the exact solution, and if the two curves were plotted on the same figure, they would be indistinguishable. This tells us that the error produced by substituting the crystal rotation in lieu of the crystal lattice rotation is compensated by the error produced by ignoring the higher-order terms of the polynomial expression for the total plastic slips (at least, for this example). This is an interesting finding since Algorithm #2 contains more assumptions that Algorithm #1, and yet it exhibits higher accuracy.

The difference between the exact and approximate solutions is a little bit more apparent in the calculated primary and secondary co-rotational slips, even though the numerical errors remain small. Figs. 11 and 12 show comparisons of the primary and secondary slips, respectively, calculated by the exact and the two approximate solutions. For clarity in presentation, we have omitted the results for Crystal Orientation #2, which are very similar to those obtained for the other two orientations. There is no clear pattern as to which of the two algorithms is more accurate, but the calculated slips are very close to the exact solution. Considering that Algorithm #2 is easier to implement and has a similar form to the incremental version used for single-slip systems, we advocate this algorithm for general-purpose large-scale calculations.

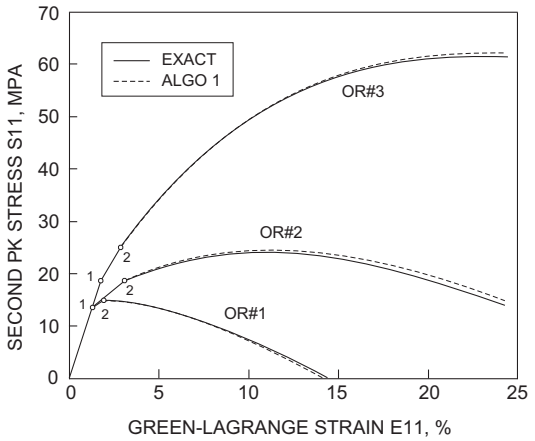

Fig. 9. Comparison of exact solutions (solid curves) and approximate solutions (dashed curves) for double-slip crystals in uniaxial tension. Approximate solutions are based on Alternative Algorithm #1. Numbers next to the open dots are slip systems activated.

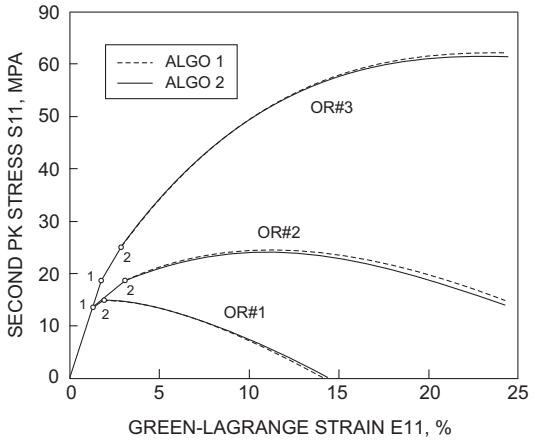

Fig. 10. Comparison of solutions calculated with Alternative Algorithms #1 and #2 for double-slip crystals in uniaxial tension. Numbers next to open dots are slip systems activated.

5.3. Hardening and multiple slips

Continuing with the same problem as in the previous example, we consider the effect of Taylor hardening on the duplex system response. To this end, we specify plastic modulus values of $\mathcal{H} = 200$, 500, and 1000, and compare the calculated overall stress–strain responses with the perfectly plastic response in Fig. 13 for Crystal Orientation #1. As the plastic modulus increases, we see that the duplex system response approaches the single-slip response. In fact, the two responses are nearly one on top of the other for the case $\mathcal{H} = 1000$. This is because, as noted in the Introduction, crystals do exhibit significantly higher hardening rates when deforming in multiple slips than when deforming in single slip, and thus, they have a propensity to deform in single slip and avoid multiple slips when the plastic modulus is high. Stated in another way, when the plastic hardening response is strong the sharing of plastic deformation between the primary and secondary slip systems becomes biased toward one of the two slip systems. In this particular example, the primary slip system becomes the dominant mechanism (although the next example reveals that this is not always the case). Fig. 14 portrays the primary co-rotational slips developed in single-slip and duplex systems plotted as functions of the Eulerian Almansi strain. As the plastic modulus increases, we see that the cumulative primary slip in a duplex system approaches the primary slip in a single-slip system, suggesting that the secondary slip approaches zero.

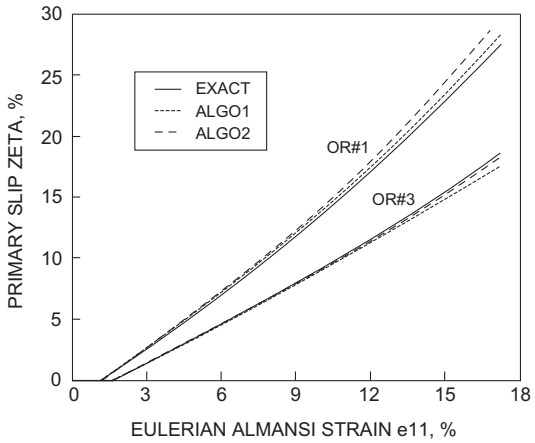

Fig. 11. Variation of co-rotational primary slip ζ versus Eulerian Almansi strain for two-slip crystals under uniaxial tension: exact versus approximate solutions.

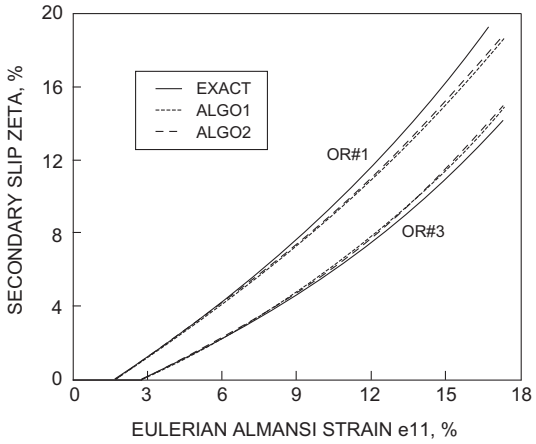

Fig. 12. Variation of co-rotational secondary slip ζ versus Eulerian Almansi strain for two-slip crystals under uniaxial tension: exact versus approximate solutions.

Next, we remove the constraints on all slip systems of an f.c.c. crystal and allow them to activate freely under the same imposed deformation field. Fig. 15 portrays the resulting stress–strain response of Crystal Orientation #3 for the case $\mathcal{H} = 0$ (perfect plasticity). When subjected to uniaxial tension, a duplex system forms right at the onset of plasticity, in which slip systems #1 and #3 activate simultaneously. This is followed by the activation of another pair of slip systems, #2 and #4. Under the assumption of small strain, the stress–strain curve would exhibit a horizontal slope; however, in the finite deformation case, we see geometric softening occurring once again, where the overall stress–strain curve exhibits a negative slope. However, the softening is not as strong as the one exhibited by Crystal Orientation #1 in spite of the fact that there are now four active slip systems.

Fig. 16 shows the influence of plastic hardening modulus $\mathcal{H}$ on the stress–strain response of Crystal Orientation #3 in single slip and four slips. As $\mathcal{H}$ increases, slip system #4 becomes more and more dominant for this crystal orientation. Thus, at $\mathcal{H} = 1000$, the stress–strain curve does not converge to the single-slip curve generated by slip system #1, even though they are still fairly close to each other. This example well demonstrates that the primary slip system does not always persist as the dominant mechanism particularly in the presence of finite deformation effects.

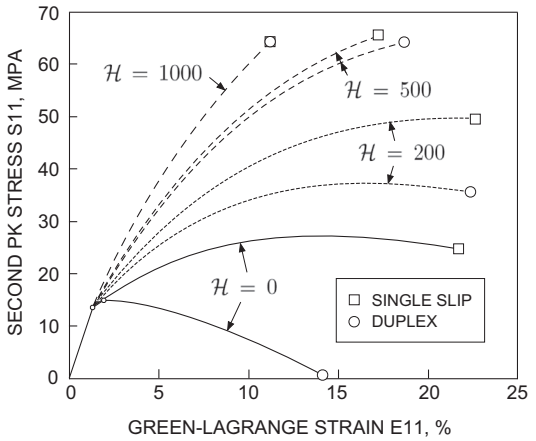

Fig. 13. Effect of Taylor hardening on the stress–strain responses of Crystal Orientation #1 under uniaxial tension: As $\mathcal{H}$ increases, the duplex system response approaches the single-slip response.

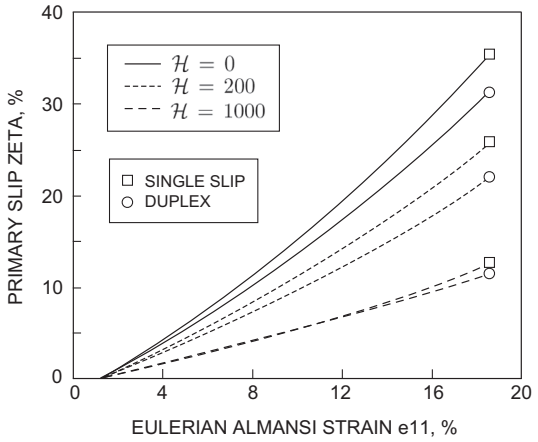

Fig. 14. Effect of Taylor hardening on the slip-strain responses of Crystal Orientation #1 under uniaxial tension: As $\mathcal{H}$ increases, the primary slips for duplex system approach the corresponding primary slips for single-slip systems.

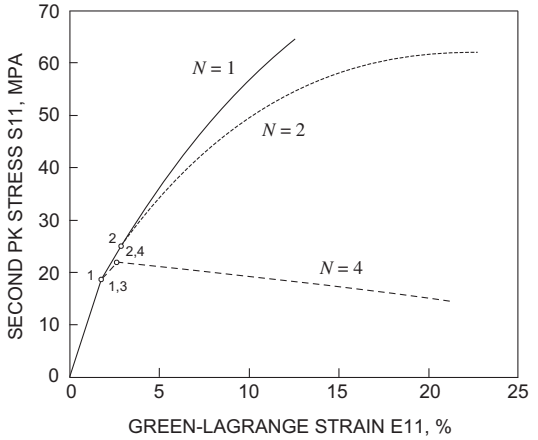

Fig. 15. Effect of multiple slips on the stress–strain responses of Crystal Orientation #3 under uniaxial tension, where $N =$ total number of active slip systems. For $N = 1$, slip systems 2, 3, and 4 were suppressed; for $N = 2$, slip systems 3 and 4 were suppressed; for $N = 4$, all available slip systems of the f.c.c. crystal were allowed to activate.

5.4. Simple shear

As a final example, we consider the following conforming displacement field applied to a crystal

$$\widetilde{u}_1 = kX_2, \quad \widetilde{u}_2 = 0, \quad \widetilde{u}_3 = 0,$$

where k is a pseudo-time variable that increases with deformation. The mode of deformation is that of simple shear. In the simulations described below, we assume that the properties of the crystal are the same as in the previous examples.

Fig. 17 portrays the resulting stress–strain responses at three different crystal orientations. We remark that in these simulations, all slip systems of an f.c.c. crystal were allowed to activate. However, the figure shows that the imposed deformation could only trigger one slip system for each crystal orientation irrespective of the magnitude of deformation. Geometric hardening is noted in the early part of the simulations, particularly with Crystal Orientation #1. This suggests that the finite rotation of the crystal (and the crystal lattice) makes it more difficult for the active system to continue slipping. We recall that Crystal Orientation #1 showed the

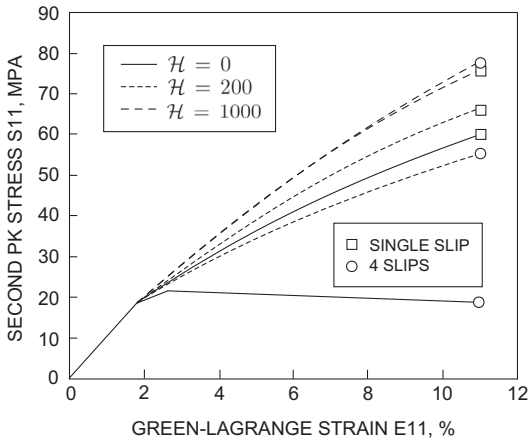

Fig. 16. Effect of Taylor hardening on the stress–strain response of Crystal Orientation #3 under uniaxial tension. In the presence of multiple slips, slip system #4 is the dominant mechanism when $\mathcal{H} = 1000$, and not the initial primary slip system #1.

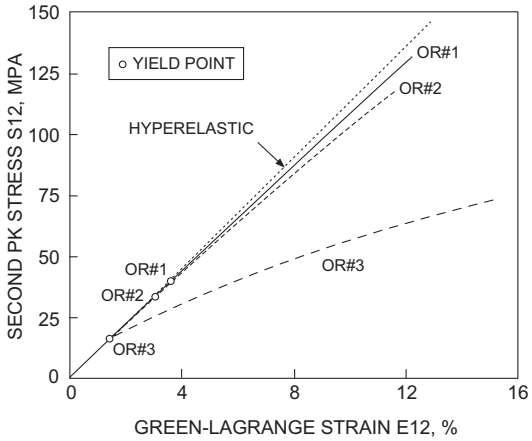

Fig. 17. Exact variation of second Piola–Kirchhoff stress component 12 versus Green–Lagrange strain component 12 for crystals subjected to simple shearing. Imposed deformation favors the development of single slip.

Table 5
Convergence profile of Newton iteration for the simple shear simulation. Displayed errors are relative norms of residual vector, normalized with respect to initial values.

Shear strain (%)	Iteration	Orientation 1	Orientation 2	Orientation 3
5	1	1.00e+00	1.00e+00	1.00e+00
	2	2.16e−06	3.44e−06	7.02e−06
	3	1.25e−12	2.36e−13	1.13e−13
10	1	1.00e+00	1.00e+00	1.00e+00
	2	1.72e−06	4.50e−06	7.76e−06
	3	1.80e−12	2.06e−13	4.42e−14
15	1	1.00e+00	1.00e+00	1.00e+00
	2	1.30e−06	6.51e−06	9.65e−04
	3	2.52e−12	1.98e−13	4.18e−12

greatest tendency to undergo geometric softening under uniaxial tension, but in the present example the opposite tendency is true. Furthermore, Crystal Orientation #3 showed the stiffest response under uniaxial tension, but under simple shear it exhibits the softest response and is the first one to yield. Since the simulations triggered only one slip system, the results reported in Fig. 17 are all exact.

Table 5 summarizes the convergence profiles of Newton iteration for the simple shear simulations. The rate of convergence is similar to that observed from the single-slip uniaxial tension example, where each load step required three iterations to fully dissipate the residual. The uniaxial tension and simple shear deformation modes can be combined to produce many different patterns of deformation, so it is reasonable to expect that the proposed algorithms will perform just as well under more complex deformation scenarios.

6. Closure

We have presented a rate-independent crystal plasticity theory in the finite deformation range using theory of distribution and strong discontinuity concepts applied to the slip systems. An important contribution of this work is the introduction of the notions of uniform and conforming deformation fields, representing the deformations of the crystal lattice and the whole crystal, respectively. An exact solution integrating the governing constitutive laws has been presented and encapsulated within the framework of the ultimate algorithm previously developed for rate-independent crystal plasticity in the infinitesimal deformation range. Alternative stress-point integration algorithms that are not exact but are much easier to implement are also presented. We advocate the linearized version of the algorithm, so-called Algorithm #2, for implementation into multipurpose finite element codes. This algorithm is simple and exhibits remarkable accuracy. In addition, it is exact in single slip, and when combined with the ultimate algorithm, it is unconditionally convergent. Implementation of Algorithm #2 in a multipurpose finite element code is currently in progress, and results will be reported upon in a future publication.

Acknowledgments

This work is supported by the U.S. Department of Energy under Grant No. DE-FG02-03ER15454 to Stanford University.

References

[1] L. Anand, M. Kothari, A computational procedure for rate-independent crystal plasticity, J. Mech. Phys. Solids 44 (1996) 525–558.
[2] M.P. Ariza, M. Ortiz, Discrete crystal elasticity and discrete dislocations in crystals, Arch Ration. Mech. Anal. 178 (2005) 149–226.
[3] F. Armero, K. Garikipati, An analysis of strand discontinuities in multiplicative finite strain plasticity and their relation with the numerical simulation of strain localization in solids, Int. J. Solids Struct. 33 (1996) 2863–2885.
[4] R.J. Asaro, Crystal plasticity, J. Appl. Mech. 50 (1983) 921–934.
[5] R.J. Asaro, J.R. Rice, Strain localization in ductile single crystals, J. Mech. Phys. Solids 25 (1977) 309–338.
[6] S. Aubry, M. Ortiz, The mechanics of deformation-induced subgrain-displocation structures in metallic crystals at large strains, Proc. R. Soc. London A 459 (2003) 3131–3158.
[7] J.F.W. Bishop, R. Hill, A theory of the plastic distortion of a polycrystal aggregate under combined stresses, Philos. Mag. 42 (1951) 414–417.
[8] J.F.W. Bishop, R. Hill, A theoretical derivation of the plastic properties of polycrystalline face-centered metal, Philos. Mag. 42 (1951) 1298–1307.
[9] R.I. Borja, H. Rahmani, Computational aspects of elasto-plastic deformation in polycrystalline solids, J. Appl. Mech. 79 (2012) 031024 (p. 9), doi: 10.1115/1.4005898.
[10] R.I. Borja, A. Aydin, Computational modeling of deformation bands in granular media, I: geological and mathematical framework, Comput. Methods Appl. Mech. Eng. 193 (2004) 2667–2698.
[11] R.I. Borja, Computational modeling of deformation bands in granular media, II: numerical simulations, Comput. Methods Appl. Mech. Eng. 193 (2004) 2699–2718.
[12] R.I. Borja, Bifurcation of elastoplastic solids to shear band mode at finite strain, Comput. Methods Appl. Mech. Eng. 191 (2002) 5287–5314.
[13] R.I. Borja, Finite element simulation of strain localization with large deformation: capturing strong discontinuity using a Petrov–Galerkin multiscale formulation, Comput. Methods Appl. Mech. Eng. 191 (2002) 2949–2978.
[14] R.I. Borja, R.A. Regueiro, Strain localization of frictional materials exhibiting displacement jumps, Comput. Methods Appl. Mech. Eng. 190 (2001) 2555–2580.

[15] R.I. Borja, A finite element model for strain localization analysis of strongly discontinuous fields based on standard Galerkin approximations, Comput. Methods Appl. Mech. Eng. 190 (2000) 1529–1549.
[16] R.I. Borja, J.R. Wren, Discrete micromechanics of elastoplastic crystals, Int. J. Numer. Methods Eng. 36 (1993) 3815–3840.
[17] B. Budiansky, T.T. Wu, Theoretical prediction of plastic strains of polycrystals, in: R.M. Rosenberg (Ed.), Proceedings of the 4th U.S. National Congress on Applied Mechanics, ASME, New York, 1962, pp. 1175–1185.
[18] E. Busso, G. Cailletaud, On the selection of active slip systems in crystal plasticity, Int. J. Plast. 21 (2005) 2212–2231.
[19] O. Cazacu, I.R. Ionescu, Augmented Lagrangian method for Eulerian modeling of viscoplastic crystals, Comput. Methods Appl. Mech. Eng. 199 (2010) 689–699.
[20] A.M. Cuitiño, M. Ortiz, Computational modelling of single crystals, Modell. Simu. Mater. Sci. Eng. 1 (1992) 225–263.
[21] Y.F. Dafalias, Plastic spin: necessity or redundancy?, Int J. Plast. 14 (1998) 909–931.
[22] S. Dumoulin, O.S. Hopperstad, T. Berstad, Investigation of integration algorithms for rate-dependent crystal plasticity using explicit finite element codes, Comput. Mater. Sci. 46 (2009) 785–799.
[23] J. Duriez, F. Darve, F.-V. Donzé, Incrementally non-linear plasticity applied to rock joint modeling, Int. J. Numer. Anal. Methods Geomech. 37 (2013) 453–477.
[24] P. Fu, S.M. Johnson, C. Carrigan, An explicitly coupled hydro-geomechanical model for simulating hydraulic fracturing in arbitrary discrete fracture networks, Int. J. Numer. Anal. Methods Geomech. 37 (2013) 2278–2300.
[25] W. Gambin, F. Barlat, Modeling of deformation texture development based on rate independent crystal plasticity, Int. J. Plast. 13 (1997) 75–85.
[26] K.S. Havner, Minimum plastic work selects the highest symmetry deformation in axially loaded f.c.c. crystals, Mech. Mater. 1 (1982) 97–111.
[27] Z. He, G. Caratini, L. Dormieux, D. Kondo, Homogenization of anisotropic elastoplastic behaviors of a porous polycrystal with interface effects, Int. J. Numer. Anal. Methods Geomech. 37 (2013) 3213–3236.
[28] R. Hill, J.R. Rice, Constitutive analysis of elastic-plastic crystals at arbitrary strain, J. Mech. Phys. Solids 20 (1972) 401–413.
[29] M.J. Hunsweck, Y. Shen, A.J. Lew, A finite element approach to the simulation of hydraulic fractures with lag, Int. J. Numer. Anal. Methods Geomech. 37 (2013) 993–1015.
[30] J.W. Hutchinson, Elastic-plastic behavior of polycrystalline metals and composites, Proc. R. Soc. London A 394 (1970) 87–119.
[31] A. Izadbakhsh, K. Inal, R.K. Mishra, Crystal plasticity based finite element modelling of large strain deformation in AM30 magnesium alloy, Modell. Simul. Mater. Sci. Eng. 20 (2012) 035016, http://dx.doi.org/10.1088/0965-0393/20/3/035016.
[32] S.R. Kalidindi, C.A. Bronkhorst, L. Anand, Crystallographic texture evolution in bulk deformation processing of fcc metals, J. Mech. Phys. Solids 40 (1992) 537–569.
[33] U.F. Kocks, The relation between polycrystal deformation and single-crystal deformation, Metall. Trans. 1 (1970) 1121–1143.
[34] U.F. Kocks, G.R. Canova, How many slip systems, and which?, in: N. Hansen, A. Horsewell, T. Leffers, H. Liholt (Eds.), Proceedings 2nd Risø International Symposium on Metallurgy and Materials Science, Deformation of Polycrystals: Mechanisms and Microstructures, Risø National Laboratory, Roskilde, Denmark, 1981, pp. 35–44.
[35] D. Kolymbas, P. Wagner, A. Blioumi, Cavity expansion in cross-anisotropic rock, Int. J. Numer. Anal. Methods Geomech. 36 (2012) 128–139.
[36] E.H. Lee, Elastic-plastic deformations at finite strains, J. Appl. Mech. 36 (1969) 1–6.
[37] T.H. Lin, Analysis of elastic and plastic strains of a face-centered cubic crystal, J. Mech. Phys. Solids 5 (1957) 143–149.
[38] C. Linder, F. Armero, Finite elements with embedded strong discontinuities for the modeling of failure in solids, Int. J. Numer. Methods Eng. 72 (2007) 1391–1433.
[39] X. Ling, M.F. Horstemeyer, G.P. Potirniche, On the numerical implementation of 3D rate-dependent single crystal plasticity formulations, Int. J. Numer. Methods Eng. 63 (2005) 548–568.
[40] F. Liu, R.I. Borja, Extended finite element framework for fault rupture dynamics including bulk plasticity, Int. J. Numer. Anal. Methods Geomech. 37 (2013) 3087–3111.
[41] F. Liu, R.I. Borja, Stabilized low-order finite elements for frictional contact with the extended finite element method, Comput. Methods Appl. Mech. Eng. 199 (2010) 2456–2471.
[42] F. Liu, R.I. Borja, An extended finite element framework for slow-rate frictional faulting with bulk plasticity and variable friction, Int. J. Numer. Anal. Methods Geomech. 33 (2009) 1535–1560.
[43] L.E. Malvern, Introduction to the Mechanics of a Continuous Medium, Prentice-Hall, Englewood Cliff, NJ, 1969.
[44] C. Miehe, S. Mauthe, F.E. Hildebrand, Variational gradient plasticity at finite strains, Part III: local-global updates and regularization techniques in multiplicative plasticity for single crystals, Comput. Methods Appl. Mech. Eng. 268 (2014) 735–762.
[45] C. Miehe, J. Schröder, A comparative study of stress update algorithms for rate-independent and rate-dependent crystal plasticity, Int. J. Numer. Methods Eng. 50 (2001) 273–298.
[46] C. Miehe, J. Schröder, J. Schotte, Computational homogenization analysis in finite plasticity. Simulation of texture development in polycrystalline materials, Comput. Methods Appl. Mech. Eng. 171 (1999) 387–418.
[47] J. Mosler, G. Meschke, 3D modelling of strong discontinuities in elastoplastic solids: fixed and rotating localization formulations, Int. J. Numer. Methods Eng. 57 (2003) 1553–1576.
[48] S. Nemat-Nasser, M. Obata, Rate-dependent finite elastic–plastic deformation of polycrystals, Proc. R. Soc. London A 407 (1986) 343–375.
[49] R.W. Ogden, Non-linear Elastic Deformations, Ellis Harwood Ltd., Chichester, U.K, 1984.
[50] M. Ortiz, E.A. Repetto, L. Stainier, A theory of subgrain displocation structures, J. Mech. Phys. Solids 48 (2000) 2077–2114.
[51] J. Pan, J.R. Rice, Rate sensitivity of plastic flow and implications for yield surface vertices, Int. J. Solids Struct. 19 (1983) 973–987.

[52] R.A. Regueiro, R.I. Borja, Plane strain finite element analysis of pressure-sensitive plasticity with strong discontinuity, Int. J. Solids Struct. 38 (2001) 3647–3672.
[53] J.R. Rice, Inelastic constitutive relations for solids: an internal-variable theory and its application to metal plasticity, J. Mech. Physics Solids 19 (1971) 433–455.
[54] J. Schröder, C. Miehe, Aspects of computational rate-independent crystal plasticity, Comput. Mater. Sci. 9 (1997) 168–176.
[55] J.C. Simo, Numerical analysis and simulation of plasticity, in: P.G. Ciarlet, J.L. Lions (Eds.), Handbook of Numerical Analysis, vol. VI, Elsevier Science B.V., 1998, pp. 183–499.
[56] J.C. Simo, J. Oliver, F. Armero, An analysis of strong discontinuities induced by strain-softening in rate-independent inelastic solids, Comput. Mech. 12 (1993) 277–296.
[57] J.C. Simo, Algorithms for static and dynamics multiplicative plasticity that preserve the classical return mapping schemes of the infinitesimal theory, Comput. Methods Appl. Mech. Eng. 99 (1992) 61–112.
[58] J.C. Simo, T.J.R. Hughes, Computational Inelasticity, Springer-Verlag, New York, NY, 1998.
[59] P. Steinmann, E. Stein, On the numerical treatment and analysis of finite deformation ductile single crystal plasticity, Comput. Methods Appl. Mech. Eng. 129 (1996) 235–254.
[60] G.I. Taylor, Plastic strain in metals, J. Inst. Metals 62 (1938) 307–324.
[61] Y. Wang, H. Fang, C.L. Zacherl, Z. Mei, S. Shang, L.-Q. Chen, P.D. Jablonski, Z.-K. Liu, First-principles lattice dynamics, thermodynamics, and elasticity of CR_2O_3, Surf. Sci. 606 (2012) 1422–1425.
[62] J.-M. Zhang, Y. Zhang, K.-W. Xu, V. Ji, Anisotropic elasticity in hexagonal crystals, Thin Solid Films 515 (2007) 7020–7024.